Luminosity function constraints on the evolution of massive red galaxies since z 0.9

Journal Item

The Astrophysical Journal, 682:919–936, 2008 August 1

LUMINOSITY FUNCTION CONSTRAINTS ON THE EVOLUTION OF MASSIVE RED GALAXIES SINCE $z \sim 0.9$

Richard J. Cool,[1] Daniel J. Eisenstein,[1] Xiaohui Fan,[1] Masataka Fukugita,[2] Linhua Jiang,[1] Claudia Maraston,[3] Avery Meiksin,[4] Donald P. Schneider,[5] and David A. Wake[6]

Received 2008 January 14; accepted 2008 April 23

ABSTRACT

We measure the evolution of the luminous red galaxy (LRG) luminosity function in the redshift range $0.1 < z < 0.9$ using samples of galaxies from the Sloan Digital Sky Survey as well as new spectroscopy of high-redshift massive red galaxies. Our high-redshift sample of galaxies is largest spectroscopic sample of massive red galaxies at $z \sim 0.9$ collected to date and covers 7 deg^2, minimizing the impact of large-scale structure on our results. We find that the LRG population has evolved little beyond the passive fading of its stellar populations since $z \sim 0.9$. Based on our luminosity function measurements and assuming a nonevolving Salpeter stellar initial mass function, we find that the most massive ($L > 3L^*$) red galaxies have grown by less than 50% (at 99% confidence), since $z = 0.9$, in stark contrast to the factor of 2–4 growth observed in the L^* red galaxy population over the same epoch. We also investigate the evolution of the average LRG spectrum since $z \sim 0.9$ and find the high-redshift composite to be well described as a passively evolving example of the composite galaxy observed at low redshift. From spectral fits to the composite spectra, we find at most 5% of the stellar mass in massive red galaxies may have formed within 1 Gyr of $z = 0.9$. While L^* red galaxies are clearly assembled at $z < 1$, $3L^*$ galaxies appear to be largely in place and evolve little beyond the passive evolution of their stellar populations over the last half of cosmic history.

Subject headings: galaxies: elliptical and lenticular, cD — galaxies: evolution — galaxies: fundamental parameters — galaxies: photometry — galaxies: statistics

Online material: color figures

1. INTRODUCTION

The favored model for the evolution of galaxies is through the hierarchical merging of smaller satellite galaxies into larger systems. The details of the frequency and efficiency of the merging process are poorly constrained, especially in the densest environments. As the endpoint of the hierarchical merging process, the most massive galaxies are most sensitive to various merger models assumptions and thus offer a strong opportunity to constrain models of galaxy formation and evolution.

Observations of the evolution of early-type galaxy stellar populations have shown that the stars in these galaxies formed at $z > 2$ and that the galaxies have had little star formation since that epoch (Bower et al. 1992; Ellis et al. 1997; Kodama et al. 1998; de Propris et al. 1999; Brough et al. 2002; Holden et al. 2005; Wake et al. 2005; Pimbblet et al. 2006; Jimenez et al. 2007; Bernardi et al. 2003a, 2003b, 2003c, 2003d, 2006; Glazebrook et al. 2004; McCarthy et al. 2004; Papovich et al. 2005; Thomas et al. 2005; Cool et al. 2006). While the average population of massive galaxies appears to be quite old and passively evolving, a number of studies have indicated that local massive early-type galaxies show signs of recent star formation activity (Trager et al. 2000; Goto et al. 2003; Fukugita et al. 2004; Balogh et al. 2005). The fraction of early-type galaxies with evidence of recent star formation seems to increase to high redshift and decreases with increasing stellar mass (Le Borgne et al. 2006; Caldwell et al. 2003; Nelan et al. 2005; Clemens et al. 2006).

At $z < 1$, early-type galaxies form a tight relationship between their rest-frame color and luminosity (the so-called color-magnitude relation or red sequence of galaxies) wherein more luminous (and hence more massive) galaxies have redder colors than less massive counterparts (Visvanathan & Sandage 1977; Bower et al. 1992; Hogg et al. 2004; McIntosh et al. 2005; Willmer et al. 2006). The tight dispersion around this relationship implies that, at fixed luminosity, galaxies on the red sequence share very similar star formations histories. If massive galaxies have undergone any mergers since $z \sim 1$, the mergers must have resulted in very little star formation; the addition of even a small fraction of blue stars would result in a larger intrinsic scatter than observed (Cool et al. 2006).

The extent to which gas-poor mergers that result in no new star formation are involved in the build-up of massive galaxies is a topic of much current research. While examples of these mergers have been observed at low redshift (Lauer 1988; van Dokkum 2005; McIntosh et al. 2007) and at intermediate redshifts (van Dokkum et al. 1999; Bell et al. 2006b; Tran et al. 2005; Rines et al. 2007; Lotz et al. 2008), the extent to which massive galaxies participate in these merger events is controversial. Bell et al. (2006a) and Le Fèvre et al. (2000) estimate that L^* red galaxies experience 0.5–2 major mergers since $z \sim 1.0$ based on pair counts of galaxies. Van Dokkum (2005) identified galaxies which have likely undergone a recent gas-poor merger based on the presence of diffuse emission extended from the main galaxies and found that 35% of today's bulge-dominated galaxies have experienced a merger with mass ratio greater than 1:4 since $z \sim 1$. Based on the very small scale correlation function of luminous red galaxies from SDSS, Masjedi et al. (2006) concluded that

[1] Steward Observatory, 933 North Cherry Avenue, Tucson, AZ 85721; rcool@as.arizona.edu.
[2] Institute for Cosmic Ray Research, University of Tokyo, 515 Kashiwa, Kashiwa City, Chiba 2778582, Japan.
[3] Institute of Cosmology and Gravitation, University of Portsmouth, Portsmouth PO1 2EG.
[4] Scottish Universities Physics Alliance, and Institute for Astronomy, Royal Observatory, University of Edinburgh, Blackford Hill, Edinburgh EH9 3HJ, UK.
[5] Department of Astronomy, Pennsylvania State University, University Park, PA 16802.
[6] Department of Physics, University of Durham, South Road, Durham, DH1 3LE, UK.

mergers between these very massive systems occur quite rarely at $z \sim 0.3$ with rates $<1/160$ Gyr^{-1}. Masjedi et al. (2008) calculate that massive early-type galaxies have grown by 1.7% per Gyr on average since $z \sim 0.2$ due to mergers with all other galaxies.

Studies based on the number counts of galaxies from COMBO-17, DEEP2, and the NOAO Deep Wide-Field Survey (NDWFS) all agree that the stellar mass averaged all red galaxies has at least doubled since $z \sim 1$ (Brown et al. 2007; Willmer et al. 2006; Bell et al. 2004). While the truncation of star formation in blue galaxies and subsequent passive fading of the stellar populations can explain the growth of L^* galaxies since $z \sim 1$, the lack of very massive blue galaxies at redshift of unity (Bell et al. 2004) indicates that any evolution of the most massive galaxies must be fueled by mergers of less luminous red galaxies and not from pure passive evolution of massive star-forming galaxies. While red galaxies with $L \approx L^*$ appear to grow substantially since $z \sim 1$, results from Brown et al. (2007) indicate that very luminous ($L \gtrsim 4L^*$) galaxies have grown by only 25% since $z \sim 1.0$. Similarly, Wake et al. (2006) used a combination of the SDSS and 2dF-SDSS LRG and QSO (2SLAQ) sample to measure the evolution of the massive galaxy luminosity functions to $z = 0.6$ and found that at least half of the massive early-type galaxies present at $z = 0.2$ must have been well assembled by $z \sim 0.6$. These investigations agree with a number of studies which have suggested little or no evolution in the most massive galaxy populations (Lilly et al. 1995; Lin et al. 1999; Chen et al. 2003; Bundy et al. 2006; Willmer et al. 2006; Cimatti et al. 2006).

In this paper we present new observations of massive red galaxies at $0.7 < z < 0.9$ and augment it with samples of massive red-sequence galaxies from SDSS in order to quantify the evolution of the massive galaxy luminosity function over half of cosmic history. Our high-redshift spectroscopic survey is unaffected by possible systematic errors from photometric redshifts and covers 7 deg^2, minimizing the effects of cosmic variance due to large-scale galaxy clustering.

After describing our galaxy sample selection criteria in § 2, we discuss the construction of our massive red galaxy luminosity functions in § 3. We interpret out luminosity function measurements Iin § 4 and examine the composite spectrum of massive red galaxies since $z \sim 0.9$ in § 5, before closing in § 6. All magnitudes discussed in the text are AB (Oke & Gunn 1983). When calculating luminosities and volumes, we use the cosmological world model of $\Omega_m = 0.25$, $\Omega_m + \Omega_\Lambda = 1$, and $H_0 = 100\,h$ km s^{-1} Mpc^{-1} (Spergel et al. 2007). When calculating time, for example when considering the aging of stellar populations, we use $h = 0.7$. All magnitudes are corrected for dust extinction using the dust maps of Schlegel et al. (1998).

2. SAMPLE CONSTRUCTION

2.1. *SDSS Galaxy Sample*

The Sloan Digital Sky Survey (SDSS; York et al. 2000; Adelman-McCarthy et al. 2008) has imaged π steradians of the sky in five bands, *ugriz* (Fukugita et al. 1996) with a dedicated 2.5 m telescope located at Apache Point Observatory (Gunn et al. 2006). Imaging is performed with a CCD mosaic in drift-scan mode (Gunn et al. 1998) with an effective exposure time of 54 s. After images are reduced (Lupton et al. 2001; Stoughton et al. 2002; Pier et al. 2003) and calibrated (Hogg, et al. 2001; Smith et al. 2002; Ivezić et al. 2004; Tucker et al. 2006), objects are chosen for follow-up spectroscopy using an automated spectroscopic fiber assignment algorithm (Blanton et al. 2003b). Two galaxy samples are selected for spectroscopy from SDSS imaging. The MAIN galaxy sample (Strauss et al. 2002) is a complete, flux-limited ($r < 17.77$), sample of galaxies with an average redshift of 0.1. The luminous red galaxy (LRG) sample (Eisenstein et al. 2001) selects luminous early-type galaxies out to $z \sim 0.5$ with $r < 19.5$ using several color-magnitude cuts in g, r, and i. The average redshift of the LRG sample is $\sim$0.3.

In addition to its contiguous coverage of the northern Galactic cap, the SDSS also conducts a deep imaging survey, SDSS Southern Survey, by repeatedly imaging an area on the celestial equator in the southern Galactic cap. The data we utilize here includes 300 deg^2 of imaging that has been observed an average of 20 times and up to 30 times. Objects detected in each observational epoch were matched using a tolerance of 0.5″ to create the final co-added catalog. The measured photometry from each epoch were combined by converting the reported *a*sinh magnitudes (Lupton et al. 1999) to flux and then calculating the mean value. Errors on each parameter are reported as the standard deviation of the flux measurements.

While the LRG color selection criteria identify massive red galaxies at moderate redshifts, at redshifts below $z \sim 0.2$ the LRG color selection becomes too permissive—underluminous blue galaxies are allowed into the sample (Eisenstein et al. 2001). In order to construct a sample of galaxies at $0.1 < z < 0.2$, we thus rely on the MAIN galaxy sample; in this redshift range, the massive galaxies of interest pass the $r < 17.77$ flux limit of the MAIN sample. We utilize a simple rest-frame color-luminosity cut, $M_g < -21$ and $(g - i)_{\rm rest} > 2$ to select low-redshift galaxies on the red sequence. These cuts result in 23,854 LRGs at $0.1 < z < 0.2$. At $0.2 < z < 0.4$, the LRG selection provides a clean sample of 46,856 massive red galaxies which we consider our intermediate-redshift galaxy sample. Our low- and intermediate-redshift samples clearly have quite different selection functions in their rest-frame colors which must be considered when measuring the evolution between samples; we address this when we present our luminosity function measurements in § 3.

2.2. *SDSS Photometry*

As described in detail in Stoughton et al. (2002,) Strauss et al. (2002), and Blanton et al. (2001) SDSS galaxy photometry is reported using two systems. Each galaxy in SDSS is fit by two seeing-convolved models, a pure de Vaucouleurs (1948) model and a pure exponential profile. The best-fitting model in the r band is used to determine the flux of the galaxy in each of the other bands by adjusting the normalization to the model while leaving all other parameters fixed to those derived in the r band. Alternatively, the Petrosian magnitude is defined to be the flux within $2\theta_{\rm P}$, where $\theta_{\rm P}$ is defined to be the radius at which point

$$\mathcal{R}_{\rm P}(\theta) \equiv \frac{\int_{0.85\theta}^{1.25\theta} d\theta'\, 2\pi\theta' I(\theta') \big/ [\pi(1.25^2 - 0.85^2)\theta^2]}{\int_0^{\theta} dr'\, 2\pi\theta' I(\theta') \big/ [\pi\theta^2]} \quad (1)$$

falls below 0.2. Here, $I(\theta)$ is the azimuthally averaged surface brightness profile of the galaxy. The Petrosian radius is determined in the r band and then applied to each of the other bands. While the Petrosian flux measurement contains a constant fraction of the galaxy's light in the absence of seeing, independent of its size or distance, model magnitudes are unbiased in the absence of color gradients and provide a higher signal-to-noise ratio (S/N) color measurement than Petrosian colors. As the Petrosian flux aperture is defined based on the shape of the light distribution, it does not require measuring the faint, low-surface brightness, isophotes of the galaxy at large radius, which is quite difficult

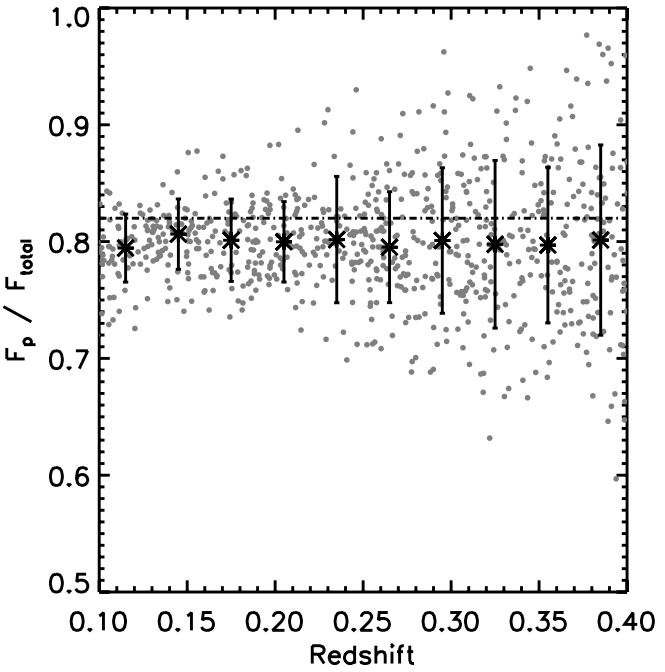

FIG. 1.—Ratio of reconstructed Petrosian flux to the total galaxy light for 2000 simulated galaxies with $M_r - 5 \log h = -22.5$, half-light radii of 12 h^{-1} kpc, and colors of a passively fading SSP formed at $z = 3$. The dark asterisks mark the mean and 1 σ dispersion of the simulations, while the gray points show each of the fake galaxy trials. We find no mean trend in the recovered flux with redshift and thus our galaxies are unaffected by overestimates of the local sky background which lead to underestimated galaxy fluxes for very large galaxies at low redshift.

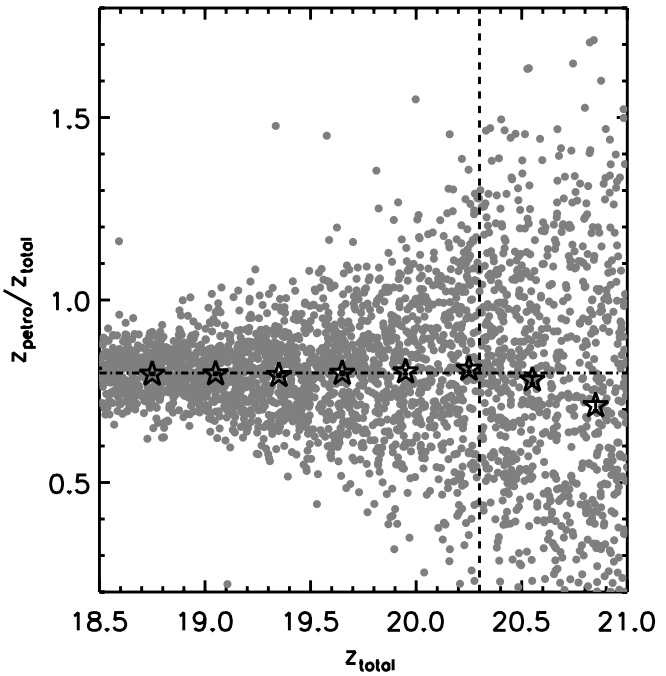

FIG. 2.—Simulation of co-added Petrosian flux measurements in high-redshift photometric data. Each gray point represents the co-added Petrosian flux from 30 realizations measured with the same method used to co-add the individual SDSS photometric epochs to generate our deep photometric catalog. The mean in bins of total flux are shown as stars. Each photometric galaxy has properties of known high-redshift massive galaxies and thus the input flux, color, and size are all correlated—the faintest galaxies in this figure are also the smallest. We find that galaxies above the z-band flux limit (*vertical dashed line*) are not strongly affected by the seeing disk; the g, r, and i bands follow similar trends. The horizontal dashed line shows the mean flux ratio measured for low-redshift simulations.

with shallow photometry. Throughout this paper, we use model magnitudes when discussing colors of galaxies and Petrosian quantities when calculating luminosities.

As has been noted by Lauer et al. (2007) SDSS photometry of very large ($r_{\rm eff} > 10''$) galaxies at low redshift have large systematic differences from measured photometry in the literature. For very large galaxies, the automated photometric pipeline includes galaxy light in the estimation of the local sky background and thus underestimates the total galaxy flux. At $z > 0.1$, we expect this effect to play a minimal role and thus perform no correction to our photometry. In order to ensure that this is a valid approach, we simulate 2000 galaxies at $0.1 < z < 0.4$ with properties of observed massive early-type galaxies. Specifically, we simulate a $M_r - 5 \log h = -22.5$ galaxy with a half-light radius of 12 h^{-1} kpc and Sersic parameter of $n = 4$. Galaxies were assigned colors assuming a passively evolving simple stellar population (SSP) that was formed in a single burst at $z = 3$. For each galaxy, we convolve the simulated postage stamp with the local seeing, apply the flat-field, bias, and bad column corrections in reverse, and add it to a raw SDSS image. Each image is then reduced using the standard SDSS PHOTO pipeline. Figure 1 shows the result of this test. We find no significant trend with redshift of the measured flux compared to the total galaxy flux, indicating that our photometry is not biased strongly due to sky subtraction errors. The mean flux ratio found in our simulations, 80%, is quite close to that expected as the Petrosian flux systematically estimates the total flux of a galaxy with a $n = 4$ surface brightness profile to be ~82% of its total flux (Graham et al. 2005). Throughout this work, we use the luminosity derived from the measured Petrosian flux directly, and thus if comparisons are done to luminosity functions based on total flux measurements, care must be taken to account for this systematic effect.

While Petrosian fluxes are unbiased in the absence of seeing, as a galaxy becomes unresolved, the Petrosian flux will report a systematically smaller fraction of the galaxy light (Blanton et al. 2001). Similarly, when working near the detection limit of our imaging, one may worry that a given object only scatters above the detection threshold a fraction of the time; an average flux across many epochs can systematically overestimate the flux of such a source. At $z > 0.7$, the sizes of our sample galaxies are approaching the size of the typical SDSS seeing disk and are quite faint relative to typical SDSS applications. To ensure that photometry of these high-redshift galaxies are unbiased, we simulate 10,000 galaxies at $z > 0.7$ with $M_r - 5 \log h = -21.5$ (corresponding to the faintest galaxies used in our luminosity function calculations in § 3), half-light radii of 8 h^{-1} kpc, and colors characteristic of a passively fading SSP which formed at $z = 3$. Using a procedure identical to that described in § 2.2, we add simulated images to raw SDSS frames and measure their photometry using PHOTO. We generate 30 realizations of the simulations with the galaxy parameters and positions held constant but allowing the Poisson noise of the fake stamp to vary between realizations. We then co-add the photometric measurements in each fake observation epoch to generate a mock co-added catalog of massive high-redshift galaxies using the same method described in § 2.1 to generate the SDSS co-added catalog. Figure 2 shows the results of this test for the SDSS z band, which is the basis of our high-redshift luminosity measurements. The gray points show each galaxy simulated in this experiment while the stars show the mean in bins of input total flux. The mean ratio of Petrosian flux to input total flux is consistent with the ratio of 80% measured for low-redshift simulations above and thus we do not expect our

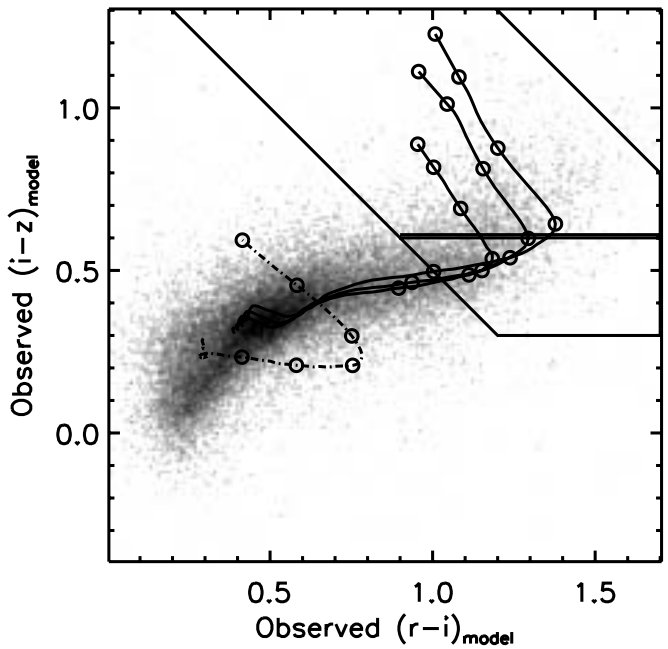

FIG. 3.—Selection of massive red galaxies at $z > 0.5$. The gray scale illustrates the observed galaxy locus for galaxies brighter than $z_{\rm model} = 20.3$ from the SDSS Southern Survey. The three solid tracks show the expected colors of passively fading galaxies from Bruzual & Charlot (2003). The reddest track in $r - i$ shows the expected colors of a very early-type galaxy and the bluest solid track shows those of an early-type disk galaxy (such as an Sa). The dot-dashed track shows the colors of an Sc type galaxy, for comparison. The tracks are marked by open circles at $\Delta z = 0.1$ intervals between redshifts of 0.5 and 1.0; the strong break in the colors occurs at $z \approx 0.7$. The boxed regions illustrate our photometric color selection. As detailed in § 2.3, galaxies at $i - z > 0.6$ are targeted at higher priority than galaxies with $0.3 < i - z < 0.6$ as the redder galaxies are most likely to reside at $z > 0.7$.

use of Petrosian quantities when measuring luminosities to bias our results to the flux limit of our survey (*vertical dashed line*). Below our selection limit, galaxies become unresolved and the total recovered flux begins to decline.

2.3. *High-Redshift Galaxy Sample*

The 54 s exposure time of SDSS imaging is not sufficient to select galaxies at $z \sim 0.9$ based on their colors. The added depth of the SDSS Southern Survey, however, allows for the selection of massive galaxies to $z \sim 1.0$. Using a similar method utilized to select LRGs at moderate redshifts from SDSS, we employ color cuts in *griz* to isolate high-redshift LRGs for spectroscopy. In designing this selection, we capitalize on the fact that the strong 4000 Å break of early-type galaxies moves through the *i*-band at $0.6 < z < 1$, resulting in progressively redder $i - z$ colors while the $r - i$ color shows less variation. Figure 3 illustrates the expected color evolution of massive galaxies at $z > 0.5$. The gray scale shows the locus of galaxy colors from the deep SDSS imaging. The solid curves show the expected evolutionary tracks for three different star formation histories; the reddest curve in $r - i$ is a very early-type SED, while the bluest track in $r - i$ is roughly an early-type spiral (e.g., an Sa) from Bruzual & Charlot (2003). Galaxies with later spectral types never get comparably red in $r - i$; for comparison, the dot-dashed track shows the color evolution of an Sc type galaxy. The open circles are separated by $\Delta z = 0.1$ with the break in the color tracks occurring at $z \sim 0.7$. Above $z \sim 0.7$, the $r - z$ color measures the distance from the turn in the color tracks and thus provides a good estimate of the photometric redshift of early-type galaxies.

We construct two regions in this color-color space to select galaxies for deep spectroscopic observations. Similarly to Eisenstein et al. (2001) we define

$$c_\perp = (r - i)_{\rm model} - (g - r)_{\rm model}/4 - 0.177. \quad (2)$$

We require every galaxy candidate to satisfy

$$i_{\rm psf} - i_{\rm model} > 0.2, \quad (3)$$

$$0.15 < c_\perp < 1.2, \quad (4)$$

$$0 < (r - i)_{\rm model} < 1.7, \quad (5)$$

$$0.3 < (i - z)_{\rm model} < 1.5, \quad (6)$$

$$17 < z_{\rm model} < 20.3, \quad (7)$$

$$1.5 < (r - z)_{\rm model} < 2.5. \quad (8)$$

Here, the magnitude and color subscripts mark if the magnitude was based on SDSS PSF magnitudes or MODEL magnitudes (Stoughton et al. 2002). Equation (3) limits targets to objects in which at least 20% of the flux arises outside a central point source to select only extended objects in the SDSS photometry. At $z = 0.9''$, $1.2''$ (the median seeing of our deep photometry) corresponds to 6.7 h^{-1} kpc, smaller than the typical luminous red galaxy, and thus we do not expect galaxies of interest to be unresolved at $0.7 < z < 0.9$. The definition of $c_\perp$ follows that of Eisenstein et al. (2001) and is designed to be parallel to the low-redshift galaxy locus in $g - r$ versus $r - i$ color-color space; equation (4) removes $z < 0.45$ interlopers from the sample.

Equations (4)–(8) limit our sample to red galaxies at $0.5 < z < 1.0$ and the flux limit imposed by equation (7) isolates only the most luminous galaxies in this redshift range. We divide our selection into two groups based on their $i - z$ color. Galaxies with $i - z > 0.6$ are given higher priority than galaxies with $0.3 < i - z < 0.6$ as the redder subset of galaxies are more likely to lie at $z > 0.7$ as shown in Figure 3. Based on early observations and data simulations, we found that our redshift success would degrade at fluxes fainter than $z_{\rm model} = 20$. In order to maximize the number of high-quality redshifts obtained, we targeted galaxies at $z_{\rm model} < 20$ at a higher priority than galaxies with $20 < z_{\rm model} < 20.3$. After target selection, fibers were allocated to 20% of the available galaxy candidates in the field.

If there are unresolved galaxies that were untargetted with our algorithm, we can quantify this sample bias by comparing the galaxy angular correlation function to the star-galaxy cross-correlation function from our targeting data. As the locations of distant galaxies are uncorrelated with Galactic stars, the presence of unresolved galaxies in our star sample will result in an apparent signal in the star-galaxy cross-correlation function due to the correlated galaxy interlopers in the sample. We construct a sample of stars which meet identical selection criteria used to select galaxies with the exception of equation (3). After masking out $2'$ regions around bright ($r < 12$) stars, we count the number of galaxy-galaxy, star-galaxy, and star-star pairs as a function of separation compared to the expected number of pairs derived from a mock catalog of objects over the same area and subject to the same bright star mask. Our spectroscopic observations directly probe the contamination by stars in our galaxy sample; we use this known contamination rate to correct for the dilution of the galaxy-galaxy autocorrelation function arising from the addition of an uncorrelated stellar sample and create the average correlation function shown in Figure 4. As expected, the star-star autocorrelation

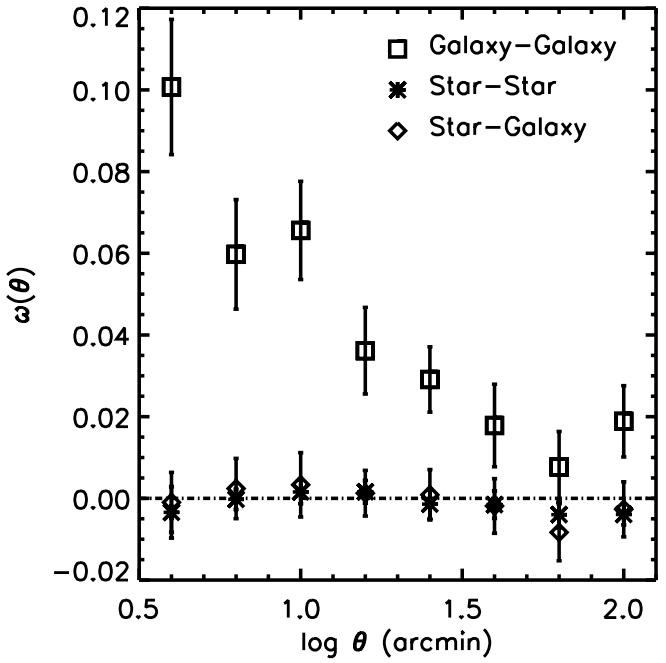

FIG. 4.—Angular correlation functions for stars and galaxies selected with our high-redshift galaxy color criteria. The galaxy-galaxy correlation function (*squares*) shows strong clustering on all scales while both the star-star autocorrelation function (*asterisks*) and star-galaxy cross-correlation function (*diamonds*) show very little clustering signal on several arcminute scales. If many galaxies were lost from our sample due to being unresolved by our star-galaxy separation, the star-galaxy cross correlation function would mirror that of the galaxy-galaxy autocorrelation function. Thus, the lack of signal at small separations in the star-galaxy cross correlation function indicates we lose, at most, 2% of our galaxy targets due to our star-galaxy separation errors.

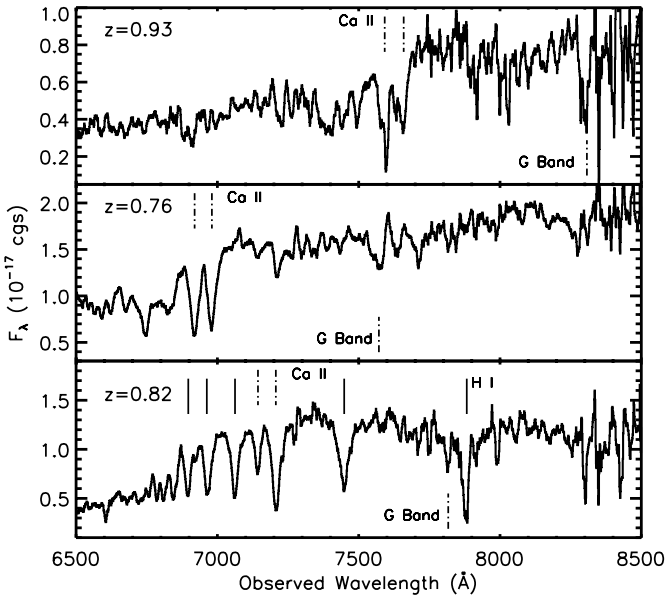

FIG. 5.—Example of MMT spectra of high-redshift galaxies. Each spectrum has been smoothed by two resolution elements for display; the spectra each have resolution of 6 Å. In each panel, vertical lines highlight prominent spectral features to guide the eye. The top panel shows a $z = 0.92$ galaxy with moderate S/N. The strong Ca II H+K absorptions lines and G band at 4300 Å allow for accurate redshift determination even at low S/N. The middle panel shows a high S/N $z = 0.76$ spectrum and the bottom panels shows a $z = 0.82$ galaxy with strong Balmer absorption features characteristic of 1 Gyr populations. The spectral range plotted was chosen to highlight the key features of our spectra; Hectospec observes considerably further into the blue, but those data are generally of quite low S/N for the high-redshift galaxies studied here.

function (*asterisks*) shows little power on several arcminute scales whereas the galaxy-galaxy autocorrelation (*squares*) function shows significant clustering. The lack of strong signal in the star-galaxy cross-correlation function implies only a small fraction of galaxies can be lost to the star sample. Based on our measurements, we find that a maximum of 3% of the star sample can be contributed by interloper galaxies at 99% confidence. As the average number density of stars in our fields is about 40% larger than galaxy targets, we find that we lose, at most, 2% of our galaxy targets due to our star-galaxy separation.

2.4. *MMT Spectroscopy Observations and Data Processing*

We observed selected galaxies using Hectospec (Fabricant et al. 1998, 2005; Roll et al. 1998), a 300 fiber spectrograph on the 6.5m MMT telescope between 2004 March and 2005 October. Hectospec offers a 1 deg^2 field of view and covers from 4000–9000 Å with 6 Å resolution. Observations were completed using seven pointings with Hectospec. For each field, approximately half of the fibers were used to target high-redshift massive red galaxy candidates and half were used to measure the faint quasar luminosity function (Jiang et al. 2006). Exposure times varied due to conditions, but each field was observed for an average of 3 hr.

All Hectospec data were reduced using the HSRED[7] package which is based upon the SDSS spectroscopic pipeline. Data were flat-fielded using observations of an illuminated screen in the dome to remove pixel-to-pixel sensitivity variations as well as to correct for the strong fringing in the Hectospec CCDs in the red. When possible, spectra of the twilight sky were taken to provide a secondary correction to account for any low-order residuals between fibers after the flat field derived from the dome flat corrections were applied. Wavelength solutions were obtained each night using observations of HeNeAr calibration lamps, and the location of strong emission lines in the spectrum of the night sky were used to correct for any drift in the wavelength solution between the observations of the calibration frames and the data frames.

Observations of each field included approximately 30 sky fibers which we used to construct the master sky spectrum from each exposure and subtract that from each object spectrum. In additional, 3–5 photometrically selected F stars were targeted in each field. The extracted spectra of these stars are compared to a grid of Kurucz (1993) model atmospheres to determine the spectral type of each star. Once we have determined the spectral type of each F star, we measure the average ratio between the observed spectra and the model prediction to determine the global calibration to convert counts pixel^{-1} to ergs s^{-1} cm^{-2} Å^{-1}. Figure 5 shows three fully processed spectra from this survey.

To determine the redshift of each object we compare the observed spectra with stellar, galaxy, and quasar template spectra and choose the template and redshift which minimizes the χ^2 between model and data. As many of our spectra have low S/Ns, every spectrum is examined by eye to ensure that the fitted redshift was correct. In cases in which the automated routine failed to converge to the correct redshift, a hand-measured redshift is used in its place. Our spectroscopy resulted in redshifts for 470 galaxies at $0.6 < z < 1.0$ over 7 deg^2 and 302 galaxies at $0.7 < z < 0.9$ which will be used in our analysis, here. Figure 6 shows the color distributions of the confirmed galaxies at $0.7 < z < 0.9$ which are used for our luminosity function calculations at high redshift.

[7] See http://mizar.as.arizona.edu/rcool/hsred.

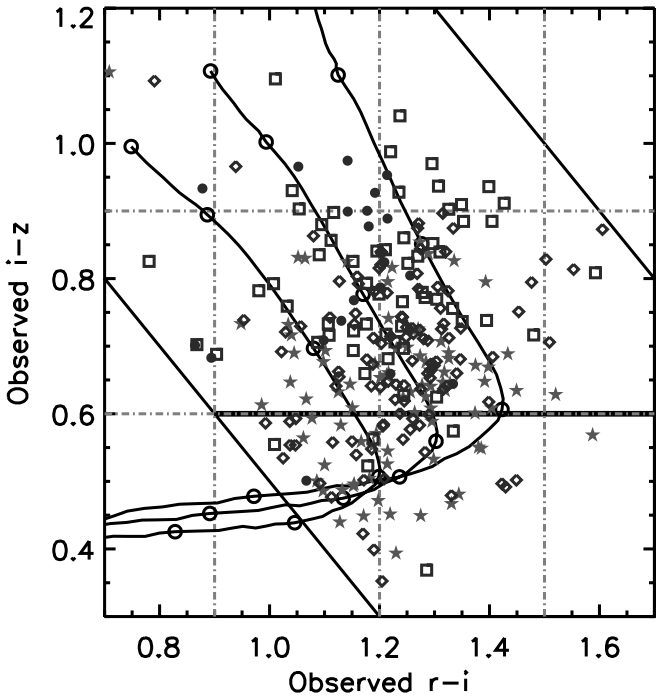

FIG. 6.—Colors of confirmed galaxies at $0.7 < z < 0.9$ from our MMT spectroscopy. The early-type galaxy color tracks and color selection criteria are as shown in Fig. 3. The colored points show the location of each of our sample galaxies in this color space; the shape of each point denotes its redshift. Stars show $0.70 < z < 0.75$ galaxies, diamonds mark $0.75 < z < 0.80$ objects, and the squares and filled circles illustrate $0.80 < z < 0.85$ and $0.85 < z < 0.90$ galaxies, respectively. The gray dot-dashed lines show the subregions of color-color space used to measure the fraction of spectroscopically observed galaxies which were excluded when evolved to our lower redshift bins. We use this correction factor when bootstrapping to our full photometric sample as described in § 3.2. [*See the electronic edition of the Journal for a color version of this figure.*]

Of the 890 galaxy candidates that were targeted for spectroscopy, 12% of the spectra did not result in a redshift measurement.

3. LUMINOSITY FUNCTION CONSTRUCTION

3.1. *Calculation of Rest-Frame Luminosities*

In order to compare the populations of massive red galaxies as a function of redshift, we first need to transform the observed photometry to the rest-frame of each galaxy to remove the effects of redshift on the observed properties. A number of approaches have been developed to perform *k*-corrections to the rest-frame system; each approach has its advantages and drawbacks. In order to minimize errors introduced due to errors in the stellar synthesis models used to calculate our *k*-corrections, we consider the rest-frame properties of our galaxies through a modified SDSS filter set. This system, denoted ${}^{0.3}u^{0.3}g^{0.3}r^{0.3}i^{0.3}z$, consists of the SDSS *ugriz* filters which have been blueshifted by a redshift of 0.3 similar to the approach used in Blanton et al. (2003a), Cool et al. (2006), and Wake et al. (2006). In this system, a galaxy at a $z = 0.3$ will have a *k*-correction that is independent of its spectral energy distribution and will equal $-2.5 \log_{10}(1 + 0.3)$. We choose a shift of 0.3 to draw upon the fact that at $z \sim 0.8$ (near the median redshift of our high-redshift galaxy sample), the observed *z*-band probes a similar portion of the spectrum as probed by the *r*-band observing a $z = 0.3$ galaxy. In the following sections, we will measure the $M_{0.3r}$ luminosity function of massive galaxies; for comparison, $B - {}^{0.3}r \approx -0.01$ for an old stellar population. Based on luminosity function fits from Brown et al. (2007) $M^*_{0.3r} - 5 \log h = -20.3$, and thus our sample focuses on galaxies with $L > 3L^*$. For reference, a $3L^*$ SSP at $z = 0.3$, which formed its stars at $z = 3$, has an approximate stellar mass of $3 \times 10^{11}\ M_\odot$.

To construct the *k*-corrections for galaxies in each of our samples, we create a grid of evolving and nonevolving SSP at solar metallicity with formation redshifts ranging from 1 to 10 from Bruzual & Charlot (2003) based on a Salpeter (1955) initial mass function (IMF). We find that this set of models adequately span the range of observed colors for all of our galaxies. Each galaxy is assigned a template based on a maximum likelihood comparison of the predicted colors and observed SDSS photometry.

While the *k*-corrections based on nonevolving models assume that the underlying stellar population remains unchanged from the observed epoch, our $k + e$ corrections include the passive evolution, normalized to $z = 0.3$, of the stellar populations in the galaxies between the observed epoch and the rest-frame redshift. For each galaxy, we use the best-fitting SSP to predict the SED the galaxy would have at $z = 0.3$; a galaxy fit by a SSP with age τ will age into a SSP with age $\tau + \Delta\tau(z_0)$, where $\Delta\tau(z_0)$ is the look-back time difference between $z = 0.3$ and z_0, the observed redshift of the galaxy. We include both types of models in order to compare the affects of passive evolution on the inferred evolution of the luminosity function of massive galaxies since $z \sim 0.9$.

3.2. *Luminosity Functions*

Luminosity functions are calculated using the standard $1/V_{\rm max}$ method (Schmidt 1968). For each galaxy, we calculate the redshifts at which the galaxy would have been selected and observed in our survey. In this calculation, we utilize the best-fit template chosen when calculating *k*-corrections, as described above, to estimate each galaxy's colors as a function of redshift. Based on these predicted colors, we assign a probability (0 or 1) that a given galaxy would have been selected at each redshift. The maximum available volume is then the integral over the redshift range weighted by the selection probability at each redshift.

Each sample is corrected independently for the spectroscopic completeness of the observations. The low-redshift SDSS MAIN and intermediate-redshift SDSS LRG galaxies were corrected to account for the spatially dependent incompleteness of SDSS spectroscopy. As we have several priority classes in our high-redshift target selection, we must correct our sample with more detail than merely the fraction of the galaxies that received fibers. Instead, we break our sample into four regions in color-magnitude space and calculate the completeness in each region independently. As described in § 2.2, galaxies were given priority based both on their $i - z$ color and $z_{\rm model}$ flux. This results in four color-magnitude regions in which we then calculate the photometric completeness by counting the number of photometrically selected galaxies which were given a fiber compared to the number of galaxies in the parent catalog in that color and magnitude bin. Our completeness correction was calculated independently for each of our seven Hectospec fields. In each field, we compare the number of spectroscopically observed objects to the total number of photometric objects within a 2 deg^2 square box around the field center when calculating our incompleteness. In doing this, we bootstrap our spectroscopic sample to 9000 photometrically selected galaxies over twice the area observed with Hectospec, thus minimizing the effects of cosmic variance on our sample. The inclusion of this photometric sample does not change the normalization of the high-redshift luminosity function we measure, but results in smaller errors due to field-to-field variations in the galaxy number counts.

S/N variations in our high-redshift galaxy spectroscopy result in approximately 12% of our observed objects with no measurable

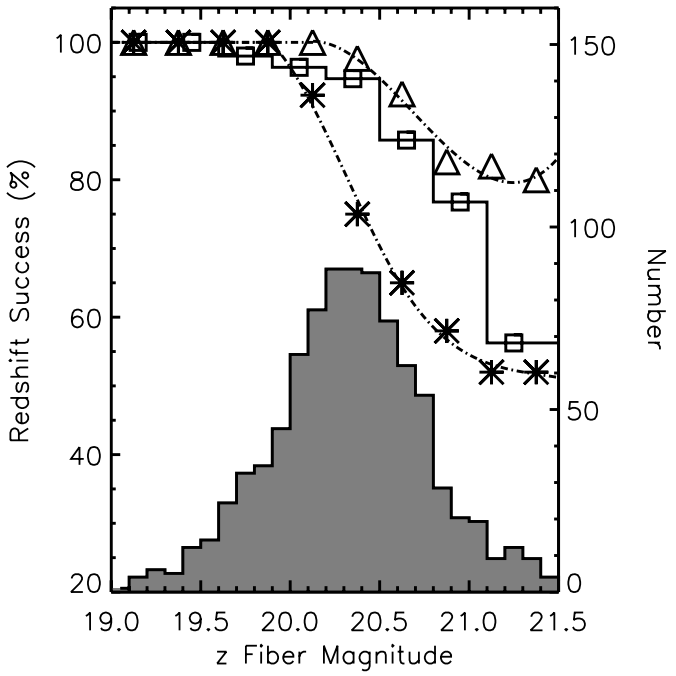

FIG. 7.—Redshift success vs. the z-band flux in a $1.5''$ aperture for two of our targeted fields. The triangles show a high-quality mask observed under photometric conditions and excellent ($\approx 0.5''$) seeing. The asterisks show a poor-quality mask affected by clouds and poor seeing leading to degraded success at the faintest fluxes. We correct for this incompleteness in each of our Hectospec fields before computing the luminosity function using low-order fits as show by the dot-dashed lines. The gray histogram illustrates the distribution of fiber magnitudes for all of our spectroscopic targets. The sharp decline in objects at $z_{\rm fiber} = 20.8$ corresponds to our sparser sampling of objects with $z_{\rm model} > 20$. The squares mark the redshift completeness of our full spectroscopic sample.

redshift. In order to correct for this effect, we measure the fraction of observed galaxies with viable redshifts as a function of the z-band flux within an $1.5''$ aperture centered on our fiber location to estimate the flux available to the spectroscopic fiber. We then fit this relationship with a low-order polynomial for each Hectospec field and apply the derived correction before calculating the the final luminosity function. Figure 7 shows an example of this technique on two different fields spanning the full range of data quality. The triangles show the completeness for a field with high S/N observed under photometric conditions and superb seeing ($\approx 0.5''$), while the asterisks show a field observed under less photometric conditions. The range in data quality leads to significant completeness variations between each of our spectroscopically observed fields; neglecting this would bias our final inferred luminosity function. The squares in the figure show the composite completeness for the full galaxy sample as a function of fiber magnitude.

We make a further correction to ensure that the galaxies utilized in the construction of the luminosity function in each redshift bin probe a homogeneous population of objects. Using the best-fit stellar population template derived when calculating the $k + e$-corrections, we estimate the colors of each galaxy as a function of redshift from $z = 0.1$ to $z = 0.9$. We then require that every galaxy included in our calculation of the luminosity function would have been selected in each of our redshift samples thus ensuring that the population of galaxies we consider at $0.1 < z < 0.2$ are consistent with galaxies at $0.7 < z < 0.9$ after the passive evolution of their stellar populations has been included. When bootstrapping to the entire photometric sample of galaxies at high redshift, we grid the $r - i$ versus $i - z$ color-color plane into 12 subsections as shown in Figure 6 and calculate the fraction of galaxies in each subregion that would be excluded based on this criterion. The size of these subregions was chosen to sample both the $i - z < 0.6$ and the $i - z > 0.6$ subsamples with similar detail. The final results are not strongly dependent on the exact subregions chosen for this correction.

When target selection is based on noisy photometry, the effects of photometric scattering of objects into or out of the nominal color- and flux-limits can be quite significant (Wake et al. 2006). As our high-redshift sample of galaxies is selected from SDSS stacked photometry, we perform an empirical test of this photometric scattering on our sample. Using the full sample of SDSS main galaxies observed at $0.1 < z < 0.2$ we create a mock sample of $0.7 < z < 0.9$ galaxies based on the best-fit $k + e$-corrections described in § 3.1. We then subject this mock galaxy sample to representative photometric errors present in our co-added photometric catalog and determine the fraction of mock galaxies that would have been selected in the presence of photometric errors. For galaxies brighter than $z = 20$, we find that $\sim$2% of selected galaxies have colors that would fall outside our color-cuts but scatter into the sample when photometric errors are included. At fainter magnitudes, $20 < z < 20.3$, approximately 10% of the galaxies included in the mock high-redshift galaxy sample have scattered above the survey flux-limit due to photometric errors. When calculating our high-redshift luminosity functions, we include these contamination rates as a statistical weight assigned to each galaxy based on its observed z-band flux.

In order to estimate the error on our high-redshift luminosity function measurements, we remove each of our spectroscopic fields (and ancillary photometric data), in turn, from our calculation of the ensemble luminosity function and repeat our calculations; we use the measured variation in the luminosity functions created with this test as an estimate of the large-scale structure error on our luminosity function measurements. Similarly, for our SDSS samples, we divide the SDSS survey area into 20 subregions and perform the same experiment. These jackknife errors are $\sim$25% larger than those based on Poisson errors alone in the lowest luminosity bins and are comparable to those estimated from counting statistics at the bright end. While subsampling can result in an underestimate of the error if a single large-scale feature is present in multiple subfields, the large area surveyed by SDSS at low redshift and the several degree separation between our spectroscopic fields at high-redshift minimize this effect and thus jackknife errors are a robust estimate of the cosmic variance errors for our samples. Throughout this paper, we utilize the larger of the two errors when doing calculations with our measured luminosity functions.

Figure 8 and Table 1 show the nonevolving luminosity function measured from our samples. The symbol (*color*) denotes the redshift bin: diamonds (*black*) $0.1 < z < 0.2$, asterisks (*magenta*) $0.2 < z < 0.3$, squares (*green*) $0.3 < z < 0.4$, and circles (*red*) $0.7 < z < 0.9$. The figure shows a clear separation between each luminosity function with higher redshift galaxies having higher luminosities (or larger number density). This characteristic behavior is expected due to the passive fading of the stellar populations in these massive red galaxies. We must remove this effect in order to understand any true changes in the underlying population of massive galaxies since $z \sim 0.9$. The turnover at low luminosities is an artifact of the color selection of these galaxies. As shown in Eisenstein et al. (2001) the LRG sample selection results in a diagonal cut across the red sequence at low luminosities which is being reflected here as the turn over at low luminosities in our luminosity function. This should not be interpreted as a characteristic luminosity of the sample. The luminosity functions

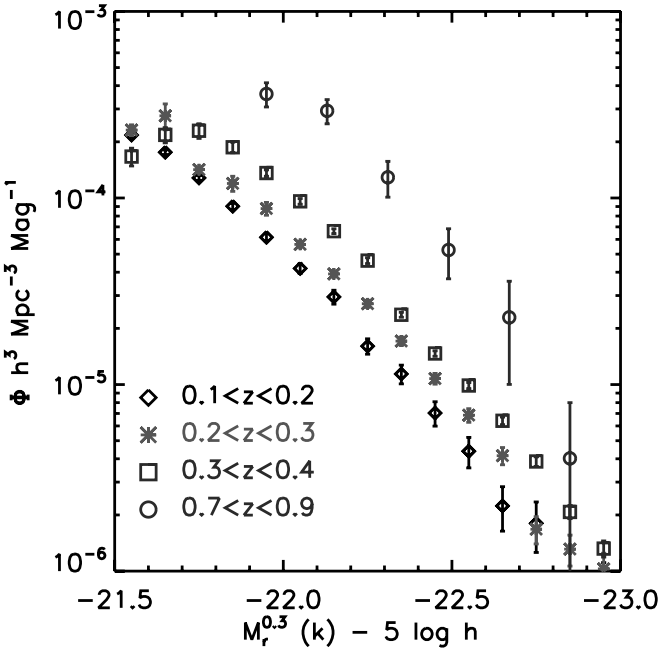

FIG. 8.—Luminosity function of massive galaxies with only a *k*-correction applied to account for the redshifting of galaxy light. The symbols mark the four redshift bins used : diamonds for $0.1 < z < 0.2$, asterisks for $0.2 < z < 0.3$, squares for $0.3 < z < 0.4$, and circles for $0.7 < z < 0.9$. The luminosity functions show the characteristic brightening toward higher redshifts due to the passive aging of stars. We must correct for the passive evolution of stellar populations in order to measure the evolution in the underlying galaxy population. [*See the electronic edition of the Journal for a color version of this figure.*]

of galaxies in our survey are shown in Figure 9 and recorded in Table 2 after the effects of evolution are included. After the effects of passive evolution are accounted for, the luminosity functions show little variation between redshift bins. The integrated luminosity densities for both the evolution-corrected and *k*-corrected luminosity functions are listed in Table 3. Analysis of these luminosity functions is the focus of § 4.

4. LUMINOSITY FUNCTION ANALYSIS

4.1. *Evolution in the Massive Galaxy Population since* $z \sim 0.9$

The agreement between the luminosity function measurements at $0.1 < z < 0.9$ as illustrated in Figure 9 indicates that the massive galaxy population has evolved little since $z \sim 0.9$. In order to quantify this evolution, we have adopted a similar parameterization to that discussed by Brown et al. (2007). Instead of measuring the evolution in the total luminosity density contained in massive galaxies, we instead measure the magnitude at which the integrated number density reaches a certain value. As massive galaxies populate the exponential tail of the luminosity distribution, small photometric errors can result in significant errors in the total luminosity density derived. For example, a shift of 3% in the luminosity threshold corresponds to a 10% change in the inferred number density of the population. Thus, if the integrated number or luminosity density at a given magnitude is used to measure the evolution of a population, results are quite sensitive to the magnitude threshold utilized. Here, we use the inverse; we measure the magnitude at which the integrated number density reaches a threshold of $10^{-4.5}$ and $10^{-5.0}$ h^3 Mpc^{-3}. These magnitudes are denoted by $M_{0.3r}(10^{-4.5})$ and $M_{0.3r}(10^{-5.0})$ throughout this discussion.

In order to measure $M_{0.3r}(10^{-4.5})$ and $M_{0.3r}(10^{-5.0})$, we fit each of our luminosity functions with a quadratic polynomial in the logarithm. We then integrate the best-fitting polynomial and

TABLE 1
LUMINOUS RED GALAXY LUMINOSITY FUNCTIONS WITH NO EVOLUTIONARY CORRECTION

	$\log_{10}$ GALAXY NUMBER DENSITY[a]			
$M_{0.3r} - 5 \log h$	$0.1 < z < 0.2$	$0.2 < z < 0.3$	$0.3 < z < 0.4)$	$0.7 < z < 0.9$
−21.55	−3.66 ± 0.01	−3.64 ± 0.03	−3.78 ± 0.05	...
−21.59	...	...	...	−3.26 ± 0.08
−21.65	−3.75 ± 0.01	−3.56 ± 0.07	−3.66 ± 0.04	...
−21.77	...	...	...	−3.30 ± 0.07
−21.75	−3.89 ± 0.01	−3.85 ± 0.01	−3.64 ± 0.04	...
−21.85	−4.04 ± 0.02	−3.92 ± 0.04	−3.73 ± 0.03	...
−21.95	−4.21 ± 0.02	−4.06 ± 0.03	−3.87 ± 0.02	...
−21.95	...	...	...	−3.44 ± 0.06
−22.13	...	...	...	−3.53 ± 0.06
−22.05	−4.38 ± 0.03	−4.25 ± 0.01	−4.02 ± 0.02	...
−22.15	−4.53 ± 0.04	−4.41 ± 0.02	−4.18 ± 0.01	...
−22.25	−4.79 ± 0.04	−4.57 ± 0.02	−4.34 ± 0.02	...
−22.31	...	...	...	−3.89 ± 0.09
−22.35	−4.94 ± 0.05	−4.77 ± 0.02	−4.63 ± 0.01	...
−22.45	−5.15 ± 0.06	−4.97 ± 0.03	−4.83 ± 0.01	...
−22.49	...	...	...	−4.28 ± 0.13
−22.55	−5.36 ± 0.08	−5.16 ± 0.04	−5.01 ± 0.02	...
−22.65	−5.65 ± 0.12	−5.38 ± 0.05	−5.19 ± 0.02	...
−22.67	...	...	...	−4.64 ± 0.24
−22.75	−5.74 ± 0.13	−5.78 ± 0.07	−5.41 ± 0.03	...
−22.85	−6.18 ± 0.22	−5.88 ± 0.08	−5.68 ± 0.03	...
−22.85	...	...	...	−5.40 ± 0.43
−22.95	−6.13 ± 0.22	−5.99 ± 0.09	−5.88 ± 0.04	...

[a] All number densities are expressed in units of h^3 Mpc^{-3} mag^{-1}.

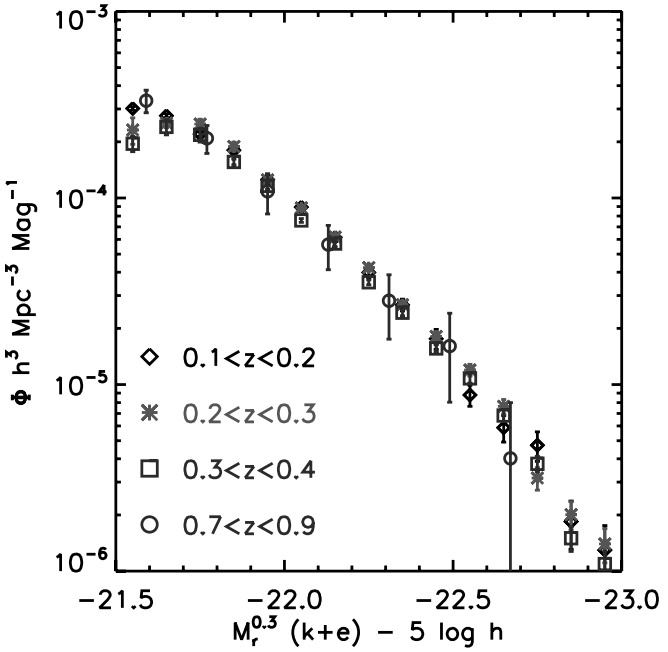

FIG. 9.—Luminosity function of massive galaxies after both the redshifting of their spectra and the passive evolution of their stellar populations have been accounted for when calculating galaxy luminosities. The symbols are as described in Fig. 8. We find very little evolution in the number counts of massive galaxies to $z \sim 0.9$, indicating that the most massive galaxies have grown little over the latter half of cosmic history. [*See the electronic edition of the Journal for a color version of this figure.*]

determine the magnitude at which the integrated number density reaches $10^{-4.5}$ and $10^{-5.0}$ h^3 Mpc^{-3}. Error bars were calculated by repeating this calculation while removing one of our subfields in turn in the same manner we calculated jackknife errors on our luminosity function measurements. The exact form we use to fit the luminosity function has little effect on our final results. Figure 10 shows the evolution in $M_{0.3r}(10^{-4.5})$ and $M_{0.3r}(10^{-5.0})$ before the passive evolution of stellar populations is removed from our galaxies, and columns (2) and (4) of Table 4 reports these measurements. Columns (2) and (6) of Table 5 and Figures 11 and 12 show the same critical magnitudes recalculated after the affects of passive evolution have been removed from our galaxy luminosity measurements. In both figures, the differences between the number density measured in each redshift bin are significant within our errors. The large area probed by SDSS makes cosmic variance between the redshift bins smaller than the observed differences at $0.1 < z < 0.4$, so large-scale structure is unlikely the cause. We fit the measured critical magnitudes with a linear evolution with redshift. The best-fit relation is shown as dot-dashed lines in Figures 11 and 12; the shaded region shows the 1 σ confidence of the fit. Fits to both critical magnitude thresholds find similar evolution; the critical magnitudes have evolved by 0.03 ± 0.08 mag between $z = 0$ and $z = 1$. When fitting this value, we add systematic floor of 0.02 mag in quadrature to each magntiude threshold. As shown by the dotted lines in the figures, the best fit to our data does not rule out pure passive evolution in the massive galaxy population.

4.2. *Importance of k-corrections on the Result*

Central to any study of the rest-frame photometric properties of extragalactic sources are the *k*-corrections used to convert the observed quantities to the rest-frame properties of the galaxy. There are a number of inherent problems with this method, in

TABLE 2
LUMINOUS RED GALAXY LUMINOSITY FUNCTIONS AFTER PASSIVE EVOLUTION CORRECTION

	$\log_{10}$ GALAXY NUMBER DENSITY[a]			
$M_{0.3r} - 5 \log h$	$0.1 < z < 0.2$	$0.2 < z < 0.3$	$0.3 < z < 0.4$	$0.7 < z < 0.9$
−21.55	−3.52 ± 0.01	−3.64 ± 0.07	−3.71 ± 0.04	...
−21.59	...	...	...	−3.48 ± 0.06
−21.65	−3.56 ± 0.01	−3.60 ± 0.02	−3.62 ± 0.04	...
−21.75	−3.66 ± 0.01	−3.60 ± 0.03	−3.66 ± 0.04	...
−21.77	...	...	...	−3.68 ± 0.07
−21.85	−3.74 ± 0.01	−3.72 ± 0.02	−3.81 ± 0.02	...
−21.95	−3.90 ± 0.01	−3.90 ± 0.01	−3.94 ± 0.02	...
−21.95	...	...	...	−3.96 ± 0.11
−22.05	−4.05 ± 0.02	−4.05 ± 0.01	−4.12 ± 0.01	...
−22.13	...	...	...	−4.25 ± 0.12
−22.15	−4.21 ± 0.02	−4.21 ± 0.01	−4.24 ± 0.02	...
−22.25	−4.40 ± 0.03	−4.37 ± 0.02	−4.45 ± 0.01	...
−22.31	...	...	...	−4.55 ± 0.16
−22.35	−4.57 ± 0.03	−4.57 ± 0.02	−4.61 ± 0.02	...
−22.45	−4.75 ± 0.05	−4.74 ± 0.03	−4.81 ± 0.02	...
−22.49	...	...	...	−4.79 ± 0.22
−22.55	−5.06 ± 0.06	−4.92 ± 0.03	−4.97 ± 0.03	...
−22.65	−5.23 ± 0.07	−5.12 ± 0.04	−5.17 ± 0.03	...
−22.67	...	...	...	−5.41 ± 0.43
−22.75	−5.33 ± 0.08	−5.50 ± 0.06	−5.42 ± 0.04	...
−22.85	−5.73 ± 0.13	−5.70 ± 0.08	−5.82 ± 0.07	...
−22.85	...	...	...	−5.40 ± 0.43
−22.95	−5.89 ± 0.15	−5.85 ± 0.09	−5.96 ± 0.08	...

[a] All number densities are expressed in units of h^3 Mpc^{-3} mag^{-1}.

TABLE 3
Integrated Luminosity Density

	$j(M_{0.3r} < -21.50)$[a]		$j(M_{0.3r} < -22.25)$[a]	
Redshift (1)	k[b] (2)	$k+e$[c] (3)	k[b] (4)	$k+e$[c] (5)
0.15.....	2.63 ± 0.04	5.45 ± 0.06	0.24 ± 0.02	0.54 ± 0.03
0.25.....	3.54 ± 0.06	5.22 ± 0.09	0.33 ± 0.01	0.54 ± 0.02
0.35.....	5.18 ± 0.11	4.58 ± 0.09	0.50 ± 0.01	0.48 ± 0.01
0.80.....	34.32 ± 10.00	5.47 ± 1.00	2.46 ± 0.62	0.71 ± 0.29

[a] Luminosity densities in units of $10^6\ h^3\ L_\odot\ \mathrm{Mpc}^{-3}$.
[b] Integrated luminosity densities based on luminosity functions derived without correcting for the passive fading of stellar populations.
[c] Integrated luminosity densities based on luminosity functions calculated after correcting for stellar evolution based on Bruzual & Charlot (2003) stellar population synthesis models and a Salpeter IMF as discussed in § 3.2.

particular when applied to the massive galaxies of interest here. As demonstrated in Eisenstein et al. (2003) and Cool et al. (2006) popular stellar synthesis models such as Bruzual & Charlot (2003) and PEGASE.2 (Fioc & Rocca-Volmerange 1999) do not match the spectral properties of LRGs, especially α-element features; LRGs are α-enhanced compared to solar while the synthesis models do not include nonsolar α-abundances. Furthermore, a number of studies (e.g. Eisenstein et al. 2001; Wake et al. 2006) demonstrate that the current generation of stellar synthesis models poorly reconstruct the observed broadband colors of galaxies on the red sequence over a variety of redshifts.

To explore the importance of the k-correction models on our inferred results, we employ a second set of k-corrections based on the Maraston (2005) models provided by C. Maraston (2007, private communication). These models were created to more accurately track the colors of massive red galaxies than simple stellar populations. The spectrum is modeled as a composite of a metal-rich ($2\ Z_\odot$) population and a metal poor ($0.005\ Z_\odot$) population; the metal-poor population holds 10% of the mass in the galaxy.

Figure 13 shows the expected colors of a passively fading galaxy from the the Maraston (2005) and Bruzual & Charlot (2003) models utilized in our analysis. As shown in the figure, at $z > 0.6$, the Maraston models predict significantly bluer $g - r$ colors, and more closely follows the observed color locus of galaxies in our sample. While the $g - r$ and $g - i$ colors of galaxies are better matched with the Maraston (2005) models, the $r - i$ colors predicted from both templates are systematically bluer than observed galaxies.

In order to understand any systematics introduced based on the stellar synthesis models used, we reperformed our analysis using the Maraston (2005) models as the basis for our $k - e$ and $k + e$ corrections. Figure 14 shows the result of this analysis compared to the low-redshift luminosity function derived using Bruzual & Charlot spectral templates. The number density of massive galaxies shows little evolution after the passive evolution of the stellar evolutions are taken into account regardless of the models used to perform the $k + e$-corrections as shown in Figures 11 and 12 and columns (4) and (7) in Table 5. There is, however, a net offset in the measured luminosity of galaxies between the two methods, so care must be taken that k-correction differences are accounted for when comparing galaxy samples from differing analysis techniques. To quantify any difference in the implied evolution based on these two sets of stellar templates, we plot both the Bruzual & Charlot and Maraston derived $M_{0.3r}(10^{-4.5})$ and $M_{0.3r}(10^{-5.0})$ in Figures 11 and 12. In both data sets, these quantities have only evolved by less than 0.05 mag since $z \sim 0.9$, implying that massive galaxies do little more than fade over the latter half of cosmic history.

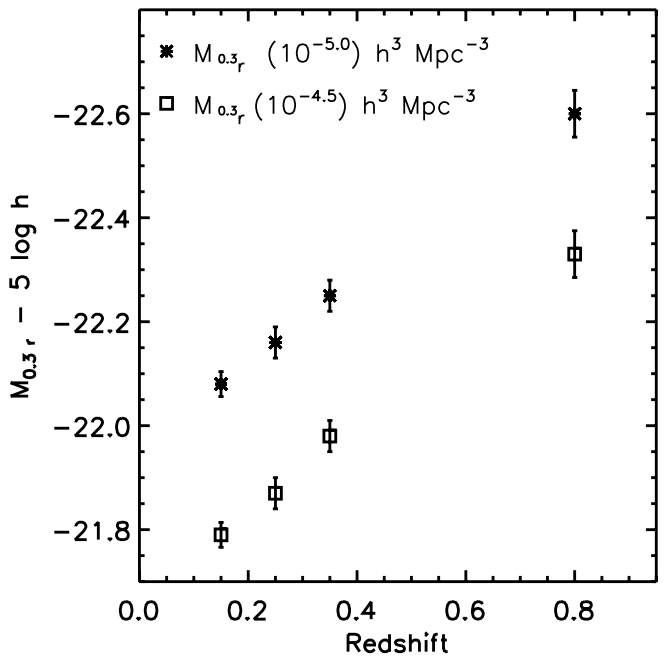

Fig. 10.—Evolution of $M_{0.3r}(10^{-4.5})$ and $M_{0.3r}(10^{-5})$, the magnitudes at which the integrated luminosity density reaches values of $10^{-4.5}\ h^3\ \mathrm{Mpc}^{-3}$ (*asterisks*) and $10^{-5.0}\ h^3\ \mathrm{Mpc}^{-3}$ (*squares*), respectively. Here, we show the evolution of this parameter if the passive fading of stellar populations is not removed when calculating galaxy luminosities. Both measurements show the characteristic brightening toward higher redshifts. Without removing the luminosity evolution induced by the passive evolution of stars in these massive galaxies, the observed trends may be due to both the passive fading of galaxies over time or the build up in the number density of these galaxies over cosmic history.

4.3. *Merger Fraction from* $z \sim 0.9$

Following the method described in Wake et al. (2006), we construct a toy model for the merger history of LRGs to constrain the merger rate of massive red galaxies since $z \sim 0.9$. Using our $0.1 < z < 0.2$ luminosity function, we create a mock sample of galaxies and then allow a fixed fraction of them to have undergone a 1:1 merger since $z = 0.9$. We then compare the luminosity function prediction for this mock sample to the observed luminosity function to determine the probability that both were drawn from the same population. Examples of predicted luminosity functions assuming different merger fractions are shown with the high-redshift data in Figure 15.

Our high-redshift luminosity function is best fit by no merging over the latter half of cosmic history. Merger rates greater than 25% are ruled out with 50% confidence, and merger rates larger than 40% are excluded at the 99% level based on our measured high-redshift luminosity function. This result agrees with previous studies based on lower redshift data and photometric redshift surveys (Brown et al. 2007; Masjedi et al. 2006, 2008; Wake et al. 2006). If less massive mergers are considered, more substantial merger rates are permitted. Performing the same experiment but instead considering 1:3 mergers, no merging is still favored, but rates as high as 40% are allowed at 50% confidence and only merger rates larger than 60% are ruled out at 99% confidence. These rate limits imply the total stellar mass in massive red galaxies from $z \sim 0.9$ must not have grown by more than 50% (at 99% confidence) in order to reproduce the observed luminosity functions.

TABLE 4
EVOLUTION OF THE MASSIVE RED GALAXY POPULATION WITHOUT CORRECTING FOR PASSIVE EVOLUTION

	$M_{0.3r}(10^{-5.0}) - 5\log h$[a]		$M_{0.3r}(10^{-4.5}) - 5\log h$[b]	
REDSHIFT (1)	Petrosian Luminosity (2)	20 h^{-1} kpc Aperture Luminosity[c] (3)	Petrosian Luminosity (4)	20 h^{-1} kpc Aperture Luminosity[c] (5)
0.15.....	-22.08 ± 0.008	-21.84 ± 0.005	-21.79 ± 0.005	-21.63 ± 0.005
0.25.....	-22.16 ± 0.010	-21.91 ± 0.010	-21.87 ± 0.010	-21.69 ± 0.010
0.35.....	-22.25 ± 0.010	-22.04 ± 0.010	-21.98 ± 0.010	-21.84 ± 0.010
0.80.....	-22.60 ± 0.090	-22.37 ± 0.020	-22.33 ± 0.052	-22.20 ± 0.033

[a] The magnitude at which the integrated number density of LRGs reaches $10^{-5.0}\ h^{-3}$ Mpc^{-3}.
[b] The magnitude at which the integrated number density of LRGs reaches $10^{-4.5}\ h^{-3}$ Mpc^{-3}.
[c] See § 4.5 for a full description of the aperture luminosity functions.

The fact that the most massive red galaxies appear to have evolved very little beyond the passive aging of their stellar populations since $z \sim 0.9$ is quite interesting. The most massive galaxies reside in the most massive dark matter halos—these halos have not remained static since $z \sim 1$. In a standard ΛCDM universe, the most massive halos ($M \gtrsim 3 \times 10^{13}\ M_{\odot}$) have grown by a factor of 2 or 3 since redshift of unity (Seo et al. 2007; Conroy et al. 2007a); one would naively estimate that the galaxies that reside in these halos would have grown, as well.

LRGs at $z = 0.3$ are known to reside in dense environments with mean clustering similar to rich groups and poor clusters (Zehavi et al. 2005). The formation and assembly of groups and clusters at $z < 1$ would naturally result in a discrepancy between the stellar mass growth of the massive central galaxy and the dark matter halo mass in which it resides. As satellite galaxies are accreted into the group or cluster halo, these satellites contribute stellar mass to the total stellar mass of the halo but not to the stellar mass of the central galaxy. The fact that galaxies with masses $M > 10^{11}\ M_{\odot}$ are observed to reside in a broad range of halo masses (McIntosh et al. 2007) may be a natural outcome of group and cluster formation.

If the lack of evolution in the number density of LRGs is due to the growth of clusters rather than the growth of the central LRG, one would expect to observe multiple LRGs within a single cluster halo. To address this hypothesis, Ho et al. (2007) performed a thorough accounting of the number of LRGs which reside in a single halo in the SDSS data set and Conroy et al. (2007b) used this multiplicity function to conclude that there are fewer LRG satellites of other LRG galaxies than predicted from *N*-body simulations. Furthermore, White et al. (2007) noted that the apparent lack of evolution in the clustering strength of massive galaxies since $z \sim 1$ implies that these galaxies themselves must be merging as the underlying dark matter distribution has undergone substantial merging during that epoch. Wake et al. (2008) measure the evolution of LRG clustering from $z = 0.55$ to $z = 0.2$ and find that it is consistent with the idea that LRGs which originally resided in different halos merged to create a single galaxy when their host haloes merged. From the measured clustering of red galaxies in the NDWFS Bootes field, White et al. (2007) estimate that one-third of the LRGs which are satellites galaxies of another LRG have merged or been destroyed between $z = 0.9$ and $z = 0.5$.

One model suggested to explain the deficit of LRG satellites suggests that the stars from late mergers onto massive galaxies feed the growth of an intracluster-light (ICL) type of extended envelope rather than the central galaxy. Conroy et al. (2007a) recently simulated the dissipationless evolution of galaxies since $z = 1$ and find that a model in which $\gtrsim$80% of the stars from merged satellites go into a low surface brightness extended stellar halo such as an ICL best predicts measurements of the galaxy stellar mass function and the observed distribution of ICL and brightest cluster galaxies in the local universe. If the total stellar content of the most massive haloes grow considerably at $z < 1$ but the accreted stellar content resides in an extended, diffuse, envelope around the central galaxy, the total luminosity function of massive galaxies as measured by our technique would remain unchanged.

It is clear from our observations that massive red galaxies evolve in a systematically different manner than L^* red galaxies. While the stellar mass in L^* red galaxies has doubled since $z = 1$, our analysis implies the mass in the $L > 3L^*$ red galaxies has grown, at most, by 50% over the same epoch. The growth of clusters and groups, including the intracluster light, may play a role in shaping the massive end of the red galaxy mass function while the

TABLE 5
EVOLUTION OF THE MASSIVE RED GALAXY POPULATION AFTER CORRECTING FOR STELLAR EVOLUTION

	$M_{0.3r}(10^{-5.0}) - 5\log h$[a]			$M_{0.3r}(10^{-4.5}) - 5\log h$[b]		
REDSHIFT (1)	Petrosian Luminosity (2)	20 h^{-1} kpc Aperture Luminosity[c] (3)	Maraston Luminosity[d] (4)	Petrosian Luminosity (5)	20 h^{-1} kpc Aperture Luminosity[c] (6)	Maraston Luminosity[d] (7)
0.15.....	-22.27 ± 0.008	-22.23 ± 0.007	-22.00 ± 0.005	-21.99 ± 0.005	-21.81 ± 0.005	-21.94 ± 0.005
0.25.....	-22.30 ± 0.010	-22.26 ± 0.010	-22.04 ± 0.010	-22.02 ± 0.010	-21.85 ± 0.010	-21.97 ± 0.010
0.35.....	-22.25 ± 0.010	-22.24 ± 0.010	-21.99 ± 0.010	-21.96 ± 0.010	-21.80 ± 0.010	-21.94 ± 0.010
0.80.....	-22.28 ± 0.056	-22.25 ± 0.080	-22.04 ± 0.060	-22.01 ± 0.053	-21.81 ± 0.037	-21.96 ± 0.075

[a] The magnitude at which the integrated number density of LRGs reaches $10^{-5.0}\ h^{-3}$ Mpc^{-3}.
[b] The magnitude at which the integrated number density of LRGs reaches $10^{-4.5}\ h^{-3}$ Mpc^{-3}.
[c] See § 4.5 for a description of the 20 h^{-1} kpc aperture luminosity function.
[d] Maraston luminosities are Petrosian flux measurements which have been $k + e$–corrected using Maraston (2005) models and are described in § 4.2.

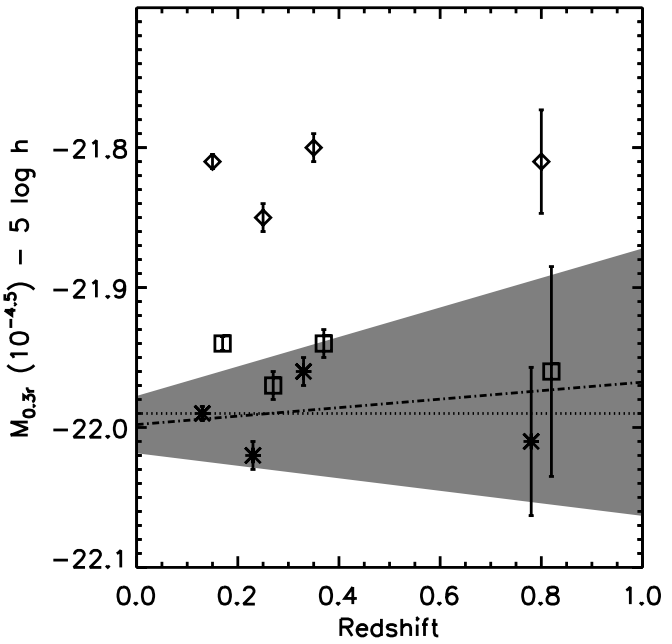

FIG. 11.—Evolution of $M_{0.3r}(10^{-4.5})$, the magnitude at which the integrated luminosity function reaches a number density of $10^{-4.5}\ h^3$ Mpc^{-3}. This parameter is used to quantify the evolution of the LRG population as these galaxies populate the exponential tail of the luminosity function and small changes to the magnitude threshold chosen may lead to significant errors when calculating the total number or luminosity density in these objects. The asterisks show measurements using the Bruzual & Charlot (2003) stellar templates, the squares show the derived evolution based on Maraston (2005) models (see § 4.2), and the diamonds show measurements based on the flux within fixed 20 h^{-1} kpc apertures and Bruzual & Charlot (2003) $k + e$ corrections as described in § 4.5. For clarity, the Bruzual & Charlot (2003) and Maraston (2005) points have been shifted by −0.02 and +0.02 in redshift, respectively. None of these samples shows a strong evolution in the massive galaxy population since $z = 0.9$. The dot-dashed line shows the best-fit linear relationship based upon the Bruzual & Charlot (2003)—derived luminosity functions and the shaded area shows the 1 σ confidence of the fit. The best-fitting slope predicts an evolution of 0.03 ± 0.08 mag between $z = 0$ and $z = 1$ and is consistent with no-evolution (*dotted line*).

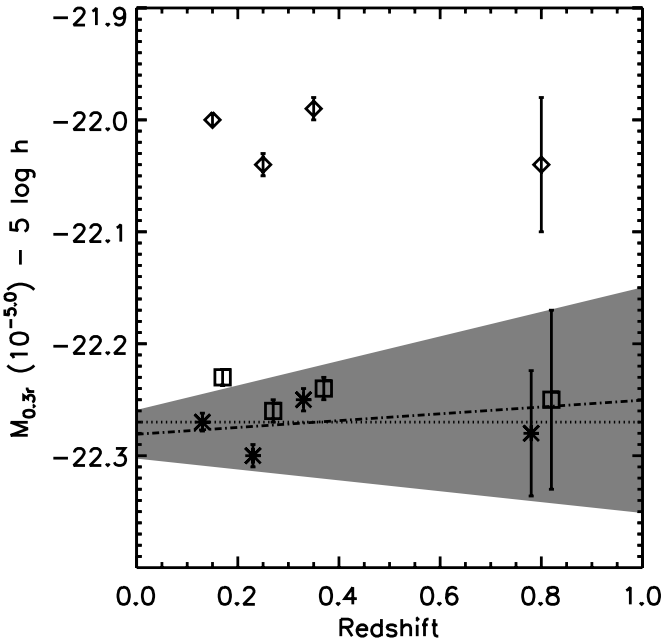

FIG. 12.—Same as Fig. 11 except showing the evolution of $M_{0.3r}(10^{-5.0})$. The best fit to the $k + e$–corrected luminosity functions based on Bruzual & Charlot (2003) models is shown, again. The fit here is independently calculated from the one in Fig. 11, but shows the same slope.

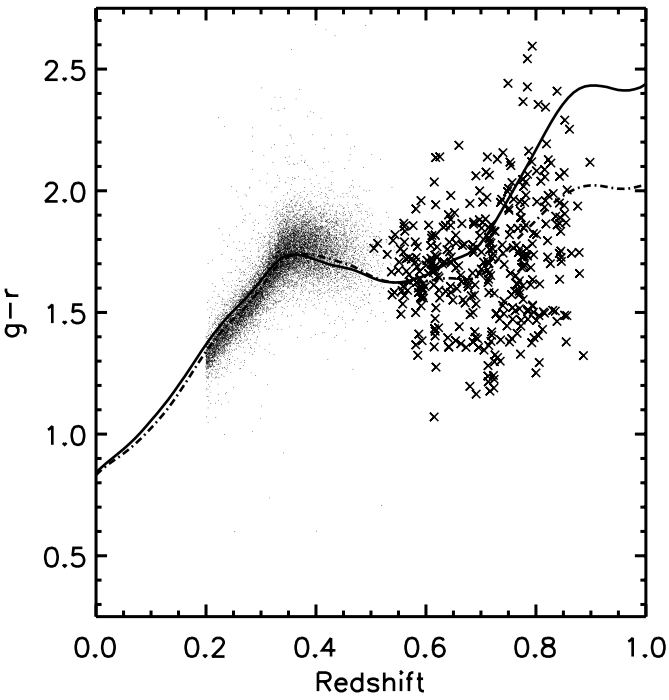

FIG. 13.—Predicted passively evolving color tracks from Bruzual & Charlot (2003) (*solid line*) and a composite stellar population based on Maraston (2005) models (*dot-dashed line*) as described in § 4.2. The data show the colors of galaxies in our intermediate and high-redshift samples. The Maraston (2005) models predict significantly bluer $g - r$ colors at high redshifts which follow the observed locus of galaxy colors more closely than Bruzual & Charlot (2003) SSP predictions.

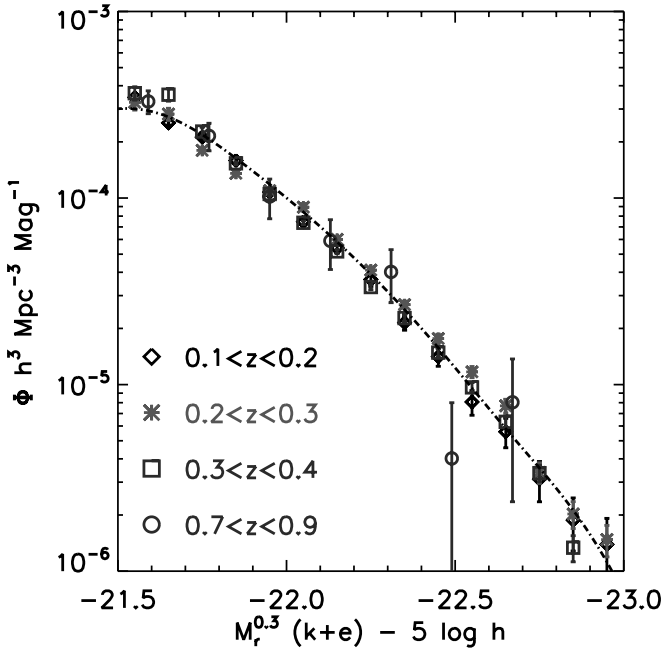

FIG. 14.—Evolution of the massive galaxy luminosity function using Maraston (2005) models when correcting for the redshifting of the galaxy spectra and the passive evolution of their stellar populations. The data points are as in Fig. 8. The dot-dashed line shows the $0.1 < z < 0.2$ luminosity function calculated using Bruzual & Charlot (2003) templates for comparison. We find no strong difference in the inferred evolution of massive galaxies when different stellar synthesis models are used. [*See the electronic edition of the Journal for a color version of this figure.*]

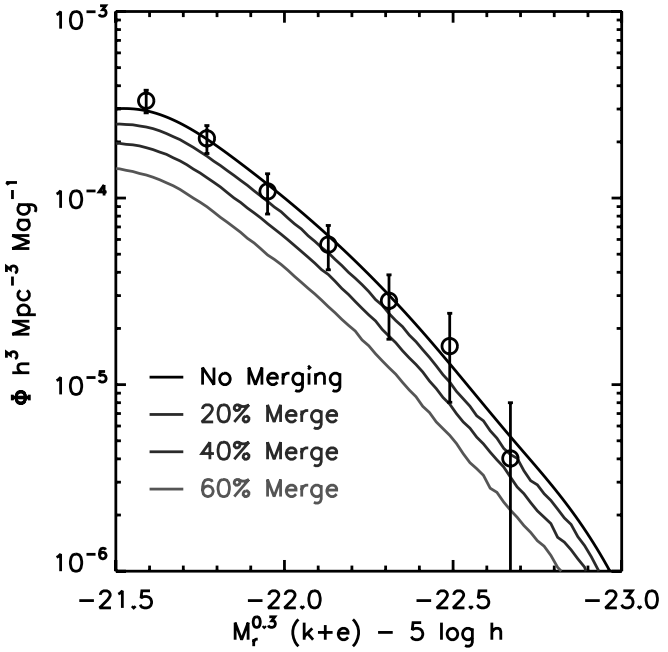

FIG. 15.—Models of the high-redshift luminosity function (*points and error bars*). Each of the solid lines shows a simulation in which our $0.1 < z < 0.2$ luminosity function is evolved backward assuming a fixed fraction of the LRGs has doubled its luminosity through 1:1 mergers between $z \sim 0.9$ and $z \sim 0.1$. Full details can be found in § 4.3. Our data are consistent with no growth in the massive red galaxy population since $z \sim 0.9$; merger fractions larger than 25% are ruled out at the 50% confidence level and merger fractions larger than 40% are ruled out at the 99% level. [*See the electronic edition of the Journal for a color version of this figure.*]

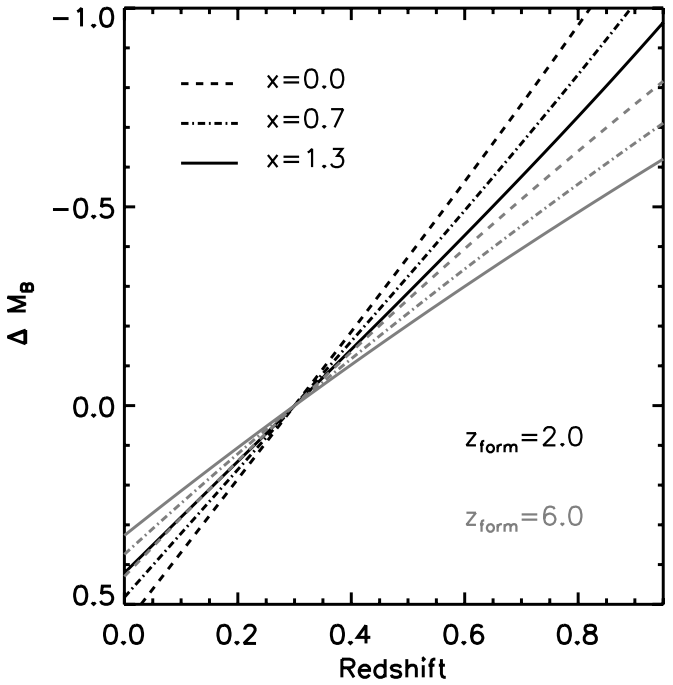

FIG. 16.—*B*-band luminosity evolution based on initial mass functions with different slopes using the fits presented in van Dokkum (2007). The gray lines show the expected evolution of an SSP formed at $z = 6$, while the black lines show the trends for $z = 2$; all of the tracks have been normalized at $z = 0.3$. If galaxies in our sample have IMF slopes shallower than the traditional $x = 1.3$ Salpeter (1955) value, we would underestimate the evolution of galaxies at $z = 0.8$ by $\gtrsim$0.15 mag by utilizing synthesis models based on the Salpeter (1955) IMF.

lower mass red galaxies are formed through the quenching of star forming galaxies at low redshifts. Alternatively, if the processes that govern star formation at the epoch of massive red galaxy formation are systematically different from those which govern star formation at $z < 1$, our analysis may underestimate the number density evolution in our sample. In the following section, we explore the impact that an evolving IMF would have on our analysis.

4.4. *Implication in the Presence of an Evolving Initial Mass Function*

Throughout all of our analyses, the slope of the stellar IMF is held fixed. While our data set is not sufficient to constrain any evolution in the IMF of massive galaxies, if this evolution exists, it can strongly affect our conclusions. Local measurements of the IMF show that at $M \gtrsim 1\ M_{\odot}$ the IMF follows a power law ($M/M_{\odot} \propto M^{-x}$; $x = 1.3$) with a turnover at lower masses (Salpeter 1955; Kroupa 2001; Chabrier 2003). For this discussion, we will only consider the IMF at $M \gtrsim 1\ M_{\odot}$; lower mass stars, while contributing significant stellar mass to the galaxy, do not contribute significantly to the galaxy luminosity and thus play a negligible role in the evolution of the M/L ratio compared to variations in more massive stars. Suggestions of top-heavy IMFs have been found in environments dominated by violent star formation (Rieke et al. 1993; McCrady et al. 2003; Figer et al. 1999; Stolte et al. 2005; Maness et al. 2007). Also, one may expect the IMF to evolve with redshift as the temperature of the cosmic microwave background begins to dominate over temperatures typically found in Galactic prestellar cores (Larson 1998). Recently, van Dokkum (2008) compared the luminosity evolution of galaxies in clusters at $0.02 < z < 0.83$, coupled with the color evolution of these systems, to test models of IMF evolution in early-type galaxies. These data prefer a logarithmic slope of $x = -0.3^{+0.4}_{-0.7}$, considerably flatter than $x = 1.3$ derived in the Milky Way disk. Similarly, Davé (2008) used hydrodynamical models of galaxy formation and observations of the correlation between galaxy stellar mass and star formation rate to $z = 2$ to suggest that the characteristic mass at which the IMF turns over, $\hat{M}$, evolves strongly with redshift: $\hat{M} = 0.5(1+z)^2\ M_{\odot}$.

To explore the importance of the assumed IMF slope on the inferred density evolution in the LRG population, we show luminosity evolution tracks predicted using the fits of van Dokkum (2008) for SSPs formed at $z = 2.0$ and $z = 6.0$ in Figure 16; the *B*-band luminosity evolution in each of the three tracks has been normalized to $z = 0.3$. The details of these models can be found in van Dokkum (2008). Briefly, these tracks show the expected luminosity evolution given three different IMF slopes using Maraston (2005) synthesis models and [Fe/H] = 0.35. For slopes shallower than $x = 1.3$, our current passive evolution correction will systematically undercorrect for the passive fading of stars which will lead to significant underestimations of the density evolution experienced by these galaxies. For example, if we underestimate the luminosity evolution from $z = 0.8$ to $z = 0.3$ by 0.2 mag, we would conclude that the massive galaxy population has evolved little since $z = 0.8$ when, in actuality, the number density of these massive systems has grown by a factor of 2. Clearly, more detailed constraints are needed on the fraction of high-mass to low-mass stars in these galaxies in order to place any evolutionary measurement into proper context.

4.5. *Measurements of Massive Galaxy Luminosity Functions Using Aperture Luminosities*

Comparisons of several recent studies of the evolution of the red galaxy luminosity function since $z \sim 1$ have revealed a number of possible systematic differences which have been attributed

to differences in the methods used to measure the total galaxy luminosities. For example, Brown et al. (2007) find that the stellar mass of the red galaxy population has grown by of a factor of 2 since $z = 1.0$, while results from DEEP2 suggest growth of a factor of 4 during the same epoch (Willmer et al. 2006; Faber et al. 2007). One alternative is to measure the luminosity of each galaxy in an aperture of fixed physical size and to study the evolution of the luminosity function based on this quantity. This method removes the systematics introduced by comparing analyses done with fixed angular size aperture or extrapolations to the total galaxy flux. Furthermore, extrapolations to a total brightness requires careful treatment of the low surface brightness outer isophotes which are quite difficult to photometer without very deep imaging. It is important to note, however, that the evolution of the luminosity within a fixed physical aperture size addresses a slightly different question than the total luminosity function; instead of tracking the total contribution of starlight, we instead focus on the growth of the stellar mass only in the inner region of the galaxy. Depending on the physical aperture size chosen, these luminosity measurements will not only be affected by the total starlight in the galaxy but also by the central concentration. Furthermore, the aperture luminosity function and total luminosity function may exhibit different evolution if the ratio of the luminosity within the physical aperture to the total galaxy luminosity changes with time. For example, the aperture to total luminosity ratio may change if significant mass is accreted at large radii or the stellar concentration evolves due to recent merger activity.

To investigate this method, we measure the evolution of the luminosity within the inner 20 h^{-1} kpc for each galaxy in our sample. We choose 20 h^{-1} kpc radii apertures as this size will enclose a majority of the galaxy light, thus minimizing the effects on color gradients and galaxy concentration on our results, and yet not be too large such that the photometric errors due to sky subtraction uncertainties become significant. For the low-redshift SDSS galaxy samples, we make use of the measured aperture fluxes at fixed angular sizes output by the SDSS pipeline. For reference, the SDSS pipeline measures galaxy flux in apertures with radii of 0.23, 0.68, 1.03, 1.76, 3.0, 4.63, 7.43, 11.42, 18.20, 28.20, 44.21, 69.00, 107.81, 168.20, and 263.00 arcseconds (see Table 7 in Stoughton et al. 2002). Based on the measured redshift of each galaxy in our sample, we interpolate the measured aperture photometry to the radius corresponding to 20 h^{-1} kpc at the redshift of the galaxy. In order to measure the fluxes of our $z \sim 0.9$ galaxies at the highest possible S/N, we photometer these galaxies directly from the SDSS imaging data. As our high-redshift sample was constructed from galaxies lying in the SDSS Southern Survey region, which has been scanned several times over the course of the survey, we construct a co-added image of 90 h^{-1} kpc $\times$ 90 h^{-1} kpc around each of our sample galaxies. Only data with seeing less than 1.5″ was used to construct the postage stamps. Before co-adding each of the individual SDSS frames, we do not account for the seeing variations between each run; this has a negligible effect on the aperture fluxes on the scales we consider here. On each co-added postage stamps, known sources were masked out to avoid contamination and the flux of each galaxy was measured in a 20 h^{-1} kpc radius aperture.

Figure 17 and Tables 6 and 7 show the aperture magnitude luminosity functions as a function of redshift. The aperture luminosity functions shown in Figure 17 show some systematic differences compared to the total luminosity functions presented in Figure 9. At fixed luminosity, the aperture luminosity function reports a systematically smaller number density than the total luminosity function. As the aperture luminosity measurements do not measure the full galaxy flux (with a median $M_{\rm aper} - M_{\rm total} \sim 0.15$ mag), the aperture luminosity function is shifted toward fainter magnitudes compared to the total luminosity function. Second, the number density falls off more rapidly toward more luminous galaxies when aperture magnitudes are considered rather than total luminosities. This appears to be due to differential aperture losses as a function of luminosity; more luminous early-type galaxies have larger effective radii and thus more flux is missed by a fixed physical size aperture. While the shape and normalization of the aperture luminosity function have systematic differences with the total luminosity function, the aperture luminosity functions show little evolution in the $0.1 < z < 0.9$ range after the effects of passive evolution are removed just as is seen for the total galaxy luminosity function.

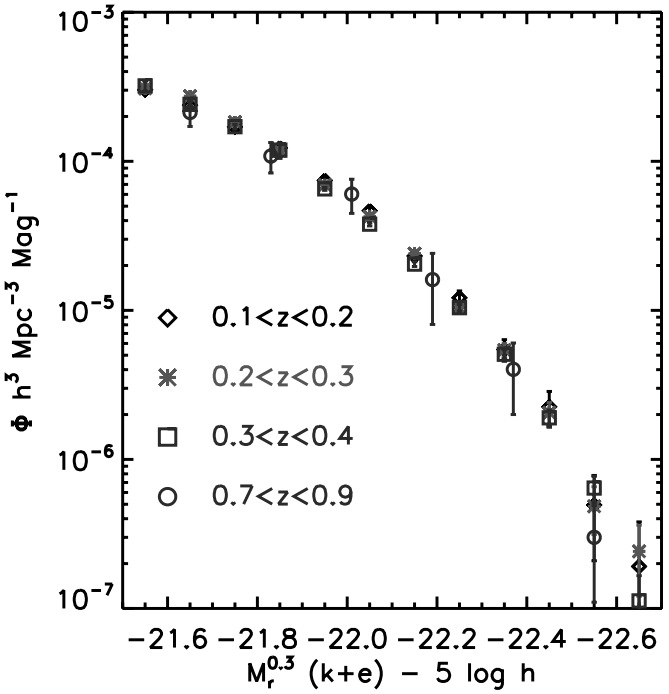

FIG. 17.—Evolution of the luminosity function based upon luminosities contained within the central 20 h^{-1} kpc of massive galaxies. No significant differences are seen when the evolution of this central flux compared to the total galaxy luminosity functions presented in Fig. 9. Measuring luminosities in apertures of fixed physical size eliminates systematic differences in estimates of the total galaxy flux and thus will allow for more robust comparisons between future samples. [*See the electronic edition of the Journal for a color version of this figure.*]

The squares in Figure 11 and values in columns (3) and (5) of Table 4 and columns (3) and (6) of Table 5 show the lack of evolution quantitatively—while the luminosities computed using physically sized apertures were systematically fainter than the total galaxy luminosities, as expected, the evolution of the central 20 h^{-1} kpc of these massive red galaxies appears to follow the evolution of the ensemble starlight. These measurements can provide a benchmark for future comparisons of the luminosity function without the need to correct for systematic differences between the photometric methods used.

5. SPECTRAL EVOLUTION OF MASSIVE GALAXIES SINCE $z \sim 0.9$

While each of our individual MMT galaxy spectra have too low S/N to perform any detailed measurements of line strengths, averaging the entire sample results in a modest quality spectrum which can be used to measure the change in the spectral structure of massive red galaxies since $z \sim 0.9$. We construct the average

TABLE 6
LRG 20 h^{-1} kpc Aperture Luminosity Functions with No Evolution Correction

	$\log_{10}$ Galaxy Number Density[a]			
$M_{0.3r} - 5\log h$	$0.1 < z < 0.2$	$0.2 < z < 0.3$	$0.3 < z < 0.4$	$0.7 < z < 0.9$
−21.55	−3.75 ± 0.01	−3.72 ± 0.01	−3.49 ± 0.04	...
−21.59	...	...	...	−3.27 ± 0.07
−21.65	−3.92 ± 0.01	−3.84 ± 0.01	−3.59 ± 0.03	...
−21.75	−4.09 ± 0.02	−3.99 ± 0.01	−3.73 ± 0.02	...
−21.77	...	...	...	−3.33 ± 0.07
−21.85	−4.30 ± 0.02	−4.12 ± 0.04	−3.88 ± 0.04	...
−21.95	−4.55 ± 0.03	−4.39 ± 0.01	−4.08 ± 0.05	...
−21.95	...	...	...	...
−22.05	−4.93 ± 0.05	−4.62 ± 0.02	−4.33 ± 0.01	−3.51 ± 0.08
−22.13	...	...	...	−3.74 ± 0.09
−22.15	−5.15 ± 0.06	−4.94 ± 0.03	−4.58 ± 0.02	...
−22.25	−5.64 ± 0.12	−5.23 ± 0.04	−4.85 ± 0.02	...
−22.31	...	...	...	−4.01 ± 0.10
−22.35	−5.93 ± 0.16	−5.52 ± 0.05	−5.18 ± 0.02	...
−22.45	−6.30 ± 0.25	−6.19 ± 0.12	−5.53 ± 0.03	...
−22.49	...	...	...	−4.53 ± 0.15
−22.55	−6.45 ± 0.43	−6.63 ± 0.19	−5.86 ± 0.04	...
−22.65	−6.64 ± 0.43	−6.63 ± 0.19	−6.20 ± 0.06	...

[a] All number densities are expressed in units of h^3 Mpc^{-3} mag^{-1}.

LRG spectra in each redshift bin used to calculate our luminosity functions presented above: $0.1 < z < 0.2$, $0.2 < z < 0.3$, $0.3 < z < 0.4$, and $0.7 < z < 0.9$. We limit the luminosity of the galaxies used in this analysis to the evolution-corrected magnitude range of $-23 < M_{0.3r} - 5\log h < -22$ to focus on galaxies for which we are very complete. After masking within 10 Åof each of the strong emission lines arising from the Earth's atmosphere, we shift the observed spectrum of each galaxy to the rest-frame and normalize it by the average flux between 4100–4200 Å. We construct the mean spectrum by weighting each individual spectrum with the same weight assigned to that galaxy when calculating the luminosity function (including the $1/V_{\max}$) and thus construct the composite spectrum of a typical galaxy in each of our redshift bins.

Figure 18 shows the co-added spectra of massive red galaxies from $z = 0.1$ to $z = 0.9$. Each of the composite spectra look quite similar showing the strong spectral features characteristic to old stellar populations. While the high-redshift composite spectrum clearly shows enhanced [O II] emission compared to the lower redshift spectra other differences between the spectra are more subtle. Figure 19 shows the measured Hδ and G band at 4300 Å absorption equivalent width, from our composite spectra. A solar-metallicity stellar population formed at $z = 2$ using a Salpeter (1955) IMF with subsequent passive fading is shown

TABLE 7
LRG 20 h^{-1} kpc Aperture Luminosity Functions after Passive Evolution Correction

	$\log_{10}$ Galaxy Number Density[a]			
$M_{0.3r} - 5\log h$	$0.1 < z < 0.2$	$0.2 < z < 0.3$	$0.3 < z < 0.4$	$0.7 < z < 0.9$
−21.55	−3.51 ± 0.01	−3.44 ± 0.02	−3.51 ± 0.02	...
−21.59	...	...	...	−3.61 ± 0.08
−21.65	−3.62 ± 0.01	−3.56 ± 0.02	−3.62 ± 0.02	...
−21.75	−3.77 ± 0.01	−3.74 ± 0.02	−3.77 ± 0.02	...
−21.77	...	...	...	−3.84 ± 0.09
−21.85	−3.91 ± 0.02	−3.93 ± 0.02	−3.93 ± 0.05	...
−21.95	−4.13 ± 0.02	−4.16 ± 0.01	−4.19 ± 0.01	...
−21.95	...	...	...	...
−22.05	−4.33 ± 0.02	−4.37 ± 0.02	−4.42 ± 0.01	−4.12 ± 0.11
−22.13	...	...	...	−4.51 ± 0.15
−22.15	−4.64 ± 0.03	−4.62 ± 0.02	−4.69 ± 0.02	...
−22.25	−4.92 ± 0.05	−4.98 ± 0.03	−4.98 ± 0.02	...
−22.31	...	...	...	−5.09 ± 0.22
−22.35	−5.26 ± 0.07	−5.27 ± 0.05	−5.29 ± 0.03	...
−22.45	−5.65 ± 0.12	−5.69 ± 0.07	−5.72 ± 0.06	...
−22.49	...	...	...	−5.81 ± 0.23
−22.55	−6.31 ± 0.25	−6.31 ± 0.15	−6.19 ± 0.09	...
−22.65	−6.72 ± 0.43	−6.62 ± 0.22	−6.95 ± 0.21	...

[a] All number densities are expressed in units of h^3 Mpc^{-3} mag^{-1}.

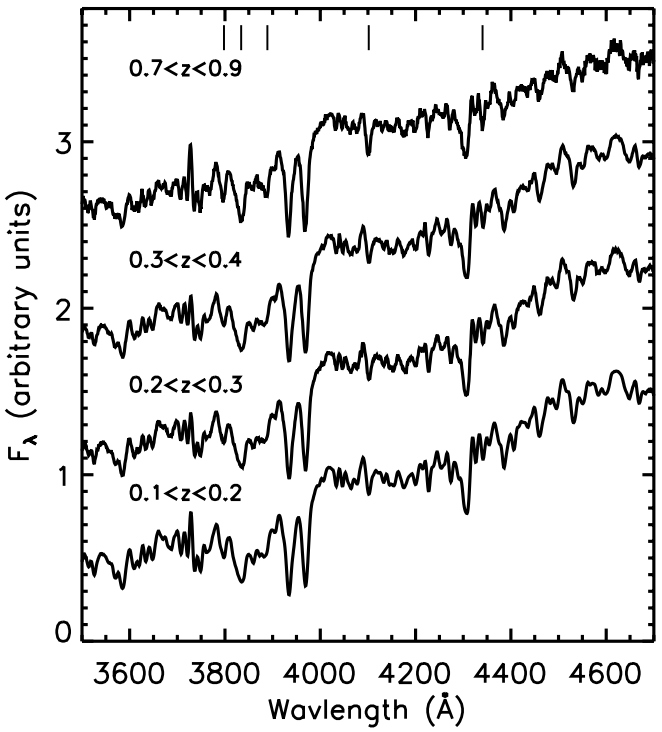

FIG. 18.—Average spectrum of LRGs since $z = 0.9$. Each composite spectrum shows features characteristic of old stellar populations, while the highest redshift spectrum shows enhanced [O II] λ3727 emission and stronger Balmer absorption indicating the presence of younger stars. The location of Balmer features are marked by vertical bars. As discussed in § 5, we model the high-redshift average spectrum with a passively faded version of the low-redshift composite combined with a recent frosting of young stars. We find at most 5% of the stellar mass in the average high-redshift LRG has formed within 1 Gyr of $z = 0.9$.

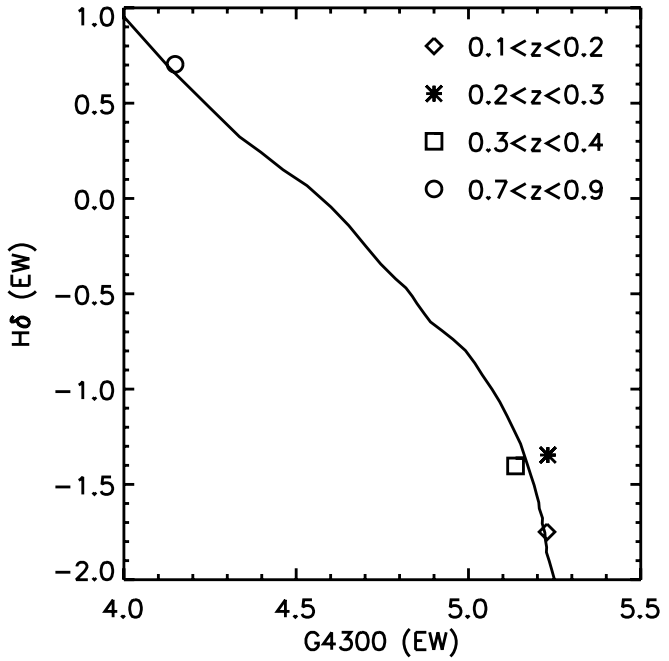

FIG. 19.—Equivalent widths of Hδ and G-band absorption features from the composite galaxy spectra. The style of data point corresponds to the redshift of the composite spectrum: $0.1 < z < 0.2$ (*diamond*); $0.2 < z < 0.3$ (*asterisk*); $0.3 < z < 0.4$ (*square*); and $0.7 < z < 0.9$ (*circle*). The solid line shows the expected trend for a solar-metallicity galaxy formed at $z = 2$ from Bruzual & Charlot (2003) models. Errors are comparable to the size of each data point. While only illustrative, the observed composite spectra show similar trends as that expected of a passively fading population.

with the solid line. Our measurements are broadly consistent with the passive fading of stars since $z \sim 0.9$. Note that we make no claim that since these points lie near the solar-metallicity track that we expect these galaxies to have solar metallicity or have a given age. It has been shown (e.g. Eisenstein et al. 2003; Cool et al. 2006) that LRGs show α-enhancements compared to solar and also that the age and metallicity of the stellar populations one might derive from most spectral indicies are degenerate. Instead, we simply illustrate that the data follow the same trend expected for a passively fading population.

In order to model the amount of recent star formation activity allowed by our high-redshift composite spectrum, we model it as the linear combination of a passively faded version of our low-redshift spectrum plus a frosting of more recent star formation activity. The lowest redshift composite is well fit by a 7.0 Gyr, solar metallicity, population. Thus, we model our high-redshift composite as the nonnegative linear sum of a 1.9 Gyr population—the universe has aged by 5.1 Gyr between $z = 0.8$ to $z = 0.15$—and a frosting of either 10 Myr, 100 Myr, or 1 Gyr stars. We find that the high-redshift composite is best modeled by a single-age population at 1.9 Gyr with no need for the presence of younger stars save for the [O II] which may be generated by either young stars or enhanced AGN activity. We can constrain the presence of 10 Myr, 100 Myr, and 1 Gyr stars to contribute less than 0.1%, 0.5%, and 5% of the stellar mass based on our spectral fits with 99% confidence. Thus, it appears that high-redshift LRGs have enhanced signatures of youth compared to their low-redshift counterparts due to the passive evolution of their stellar populations. We find no signatures of more recent star formation activity in our high-redshift sample indicative of recent gas-rich mergers at $z \sim 0.9$.

The evolution of the average spectrum presented here may be underestimated in the event that galaxies with weak absorption lines are preferentially removed from the sample due to redshift determination failures. We do not expect our spectroscopy to be biased in this way, however. Primarily, as the absorption line strength is correlated with the total galaxy luminosity, we expect the galaxies with weak lines to have luminosities fainter than the limits imposed in creating our composite spectra. Second, we would expect the presence on [O II] emission to allow redshift determination even if the absorption lines were very weak. To examine this effect, we refit each of our galaxies after masking out the wavelengths affected by the [O II] emission line and find that only three of the galaxies in our sample had sufficiently weak absorption lines that the presence of [O II] dominated the redshift fitting.

6. CONCLUSIONS

Massive galaxies serve as probes of the merger history of the universe as these galaxies have participated most heavily in the merger process. Using samples of massive ($L > 3L^*$) red galaxies observed by SDSS at low redshift augmented with a new spectroscopic sample of galaxies targeted from deep SDSS coadded photometry and observed with the MMT, we have measured the evolution of massive red galaxies at $0.1 < z < 0.9$. Our sample is currently the largest collection of massive red galaxies spectroscopically observed at $z \sim 0.9$ and thus provides an excellent tool for constraining the evolution of the most massive galactic systems over half of cosmic history.

After correcting for passive evolution using a nonevolving Salpeter (1955) IMF, we find the magnitude at which the integrated number density of the LRG population has reached $10^{-4.5}\,h^3$ Mpc^{-3} is consistent with constant with a best-fit evolution

of 0.03 ± 0.08 mag from $z = 1$ to $z = 0$. Simple toy models for the merger histories of massive red galaxies indicate that 1:1 merger rates larger than 25% are disfavored at 50% confidence and merger rates larger than 40% are ruled out at 99% significance. Even if lower mass mergers are considered, we find that the total stellar mass contained in massive red galaxies must not have grown by more than $\sim$50% since $z = 0.9$. This growth rate starkly contrasts the factor of 2–4 in stellar mass growth observed in L^* red galaxies over the same epoch. The processes that regulate the growth of massive red galaxies and yet allow the large growth observed in the L^* red galaxy population are poorly understood. As the most massive galaxies reside in group and cluster sized haloes, the processes that govern the assembly of clusters or the growth or an intracluster stellar envelope may play an important role in the shaping of LRGs.

The evolution in the average LRG spectrum to high redshift also supports a purely passive fading of LRGs since $z \sim 0.9$. The composite spectrum of our high-redshift LRGs is well described by a passively faded version of the average galaxy spectrum at $0.1 < z < 0.2$. No recent star formation is needed to explain our composite spectrum at $z = 0.9$; we constrain the mass fraction of 10 Myr, 100 Myr, and 1 Gyr stars to be less than 0.1%, 0.5%, and 5% with 99% confidence. Star formation in these LRGs must have completely ended by $z \sim 0.9$ and very few blue stars must have been accreted since that epoch.

While our sample comprises the largest spectroscopic sample of massive red galaxies at $z \sim 0.9$ collected to date, a sample of 300 galaxies suffers from small numbers of objects per luminosity bin, especially at the highest masses. Future surveys aiming to collect spectroscopic samples of many thousand LRGs at redshifts up to $z \sim 0.7$, while at slightly lower redshifts, will have the statistics to place tighter constraints on the overall density evolution of the massive red galaxy population as well as to study the evolution in the LRG luminosity function shape to constrain the role of mass-dependent processes which regulate LRG growth.

We thank the anonymous referee for a thorough and critical review of this work. R. J. C. and D. J. E. were supported by National Science Foundation grant AST 04-07200. X. F. was supported by NSF grant AST 03-07384. Observations reported here were obtained at the MMT Observatory at the Smithsonian Institution and the University of Arizona. Both the MMT staff and the Hectospec support team were instrumental in completing this work. This research made use of the NASA Astrophysics Data System.

Funding for the SDSS and SDSS-II has been provided by the Alfred P. Sloan Foundation, the Participating Institutions, the National Science Foundation, the US Department of Energy, the National Aeronautics and Space Administration, the Japanese Monbukagakusho, the Max Planck Society, and the Higher Education Funding Council for England. The SDSS Word Wide Web Site is http://www.sdss.org.

The SDSS is managed by the Astrophysical Research Consortium for the Participating Institutions. The Participating Institutions are the American Museum of Natural History, Astrophysical Institute Potsdam, University of Basel, University of Cambridge, Case Western Reserve University, University of Chicago, Drexel University, Fermilab, the Institute for Advanced Study, the Japan Participation Group, Johns Hopkins University, the Joint Institute for Nuclear Astrophysics, the Kavli Institute for Particle Astrophysics and Cosmology, the Korean Scientist Group, the Chinese Academy of Sciences (LAMOST), Los Alamos National Laboratory, the Max-Planck-Institute for Astronomy (MPIA), the Max-Planck-Institute for Astrophysics (MPA), New Mexico State University, Ohio State University, University of Pittsburgh, University of Portsmouth, Princeton University, the United States Naval Observatory, and the University of Washington.

REFERENCES

Adelman-McCarthy, J. K., et al. 2008, ApJS, 175, 297
Balogh, M. L., Miller, C., Nichol, R., Zabludoff, A., & Goto, T. 2005, MNRAS, 360, 587
Bell, E. F., Phleps, S., Somerville, R. S., Wolf, C., Borch, A., & Meisenheimer, K. 2006a, ApJ, 652, 270
Bell, E. F., et al. 2004, ApJ, 608, 752
———. 2006b, ApJ, 640, 241
Bernardi, M., Nichol, R. C., Sheth, R. K., Miller, C. J., & Brinkmann, J. 2006, AJ, 131, 1288
Bernardi, M., et al. 2003a, AJ, 125, 1817
———. 2003b, AJ, 125, 1849
———. 2003c, AJ, 125, 1866
———. 2003d, AJ, 125, 1882
Blanton, M. R., Lin, H., Lupton, R. H., Maley, F. M., Young, N., Zehavi, I., & Loveday, J. 2003a, AJ, 125, 2276
Blanton, M. R., et al. 2001, AJ, 121, 2358
———. 2003b, ApJ, 592, 819
Bower, R. G., Lucey, J. R., & Ellis, R. S. 1992, MNRAS, 254, 589
Brough, S., Collins, C. A., Burke, D. J., Mann, R. G., & Lynam, P. D. 2002, MNRAS, 329, L53
Brown, M. J. I., Dey, A., Jannuzi, B. T., Brand, K., Benson, A. J., Brodwin, M., Croton, D. J., & Eisenhardt, P. R. 2007, ApJ, 654, 858
Bruzual, G., & Charlot, S. 2003, MNRAS, 344, 1000
Bundy, K., et al. 2006, ApJ, 651, 120
Caldwell, N., Rose, J. A., & Concannon, K. D. 2003, AJ, 125, 2891
Chabrier, G. 2003, PASP, 115, 763
Chen, H.-W., et al. 2003, ApJ, 586, 745 2004, Nature, 430, 184
Cimatti, A., Daddi, E., & Renzini, A. 2006, A&A, 453, L29
Clemens, M. S., Bressan, A., Nikolic, B., Alexander, P., Annibali, F., & Rampazzo, R. 2006, MNRAS, 370, 702
Conroy, C., Ho, S., & White, M. 2007b, MNRAS, 379, 1491
Conroy, C., Wechsler,R. H., & Kravtsov, A. V. 2007a, ApJ, 668, 826
Cool, R. J., Eisenstein, D. J., Johnston, D., Scranton, R., Brinkmann, J., Schneider, D. P., & Zehavi, I. 2006, AJ, 131, 736
Davé, R. 2008, MNRAS, 385, 147
de Propris, R., Stanford, S. A., Eisenhardt, P. R., Dickinson, M., & Elston, R. 1999, AJ, 118, 719
de Vaucouleurs, G. 1948, Ann. d'Astrophy., 11, 247
Eisenstein, D. J., et al. 2001, AJ, 122, 2267
———. 2003, ApJ, 585, 694
Ellis, R. S., Smail, I., Dressler, A., Couch, W. J., Oemler, A. J., Butcher, H., & Sharples, R. M. 1997, ApJ, 483, 582
Faber, S. M., et al. 2007, ApJ, 665, 265
Fabricant, D. G., Hertz, E. N., Szentgyorgyi, A. H., Fata, R. G., Roll, J. B., & Zajac, J. M. 1998, Proc. SPIE, 3355, 285
Fabricant, D., et al. 2005, PASP, 117, 1411
Figer, D. F., Kim, S. S., Morris, M., Serabyn, E., Rich, R. M., & McLean, I. S. 1999, ApJ, 525, 750
Fioc, M., & Rocca-Volmerange , B. 1999, preprint (astro-ph/9912179)
Fukugita, M., Ichikawa, T., Gunn, J. E., Doi, M., Shimasaku, K., & Schneider, D. P. 1996, AJ, 111, 1748
Fukugita, M., Nakamura, O., Turner, E. L., Helmboldt, J., & Nichol, R. C. 2004, ApJ, 601, L127
Glazebrook, K., et al. 2004, Nature, 430, 181
Goto, T., et al. 2003, PASJ, 55, 771
Graham, A. W., Driver, S. P., Petrosian, V., Conselice, C. J., Bershady, M. A., Crawford, S. M., & Goto, T. 2005, AJ, 130, 1535
Gunn, J. E., et al. 1998, AJ, 116, 3040
———. 2006, AJ, 131, 2332
Ho, S., Lin, Y.-T., Spergel, D., & Hirata, C. M. 2007, preprint (arXiv: 0706.0727)
Hogg, D. W., Finkbeiner, D. P., Schlegel, D. J., & Gunn, J. E. 2001, AJ, 122, 2129
Hogg, D. W., et al. 2004, ApJ, 601, L29
Holden, B. P., et al. 2005, ApJ, 626, 809

Ivezić, Ž., et al. 2004, Astron. Nachr., 325, 583
Jiang, L., et al. 2006, AJ, 131, 2788
Jimenez, R., Bernardi, M., Haiman, Z., Panter, B., & Heavens, A. F. 2007, ApJ, 669, 947
Kodama, T., Arimoto, N., Barger, A. J., & Arag'on-Salamanca, A. 1998, A&A, 334, 99
Kroupa, P. 2001, MNRAS, 322,231 Kuntschner, H., & Davies, R. L. 1998, MNRAS, 295, L29
Kurucz, R. 1993, CD-ROM 13, ATLAS9 Stellar Atmosphere Programs and 2 km/s grid (Cambridge: SAO), 13
Larson, R. B. 1998, MNRAS, 301, 569
Lauer, T. R. 1988, ApJ, 325, 49
Lauer, T. R., et al. 2007, ApJ, 662, 808
Le Borgne, D., et al. 2006, ApJ, 642, 48
Le Fèvre, O., et al. 2000, MNRAS, 311, 565
Lilly, S. J., Tresse, L., Hammer, F., Crampton, D., & Le Fevre, O. 1995, ApJ, 455, 108
Lin, H., Yee, H. K. C., Carlberg, R. G., Morris, S. L., Sawicki, M., Patton, D. R., Wirth, G., & Shepherd, C. W. 1999, ApJ, 518, 533
Lotz, J. M., et al. 2008, ApJ, 672, 177
Lupton, R. H., Gunn, J. E., Ivezić, Z., Knapp, G. R., Kent, S. & Yasuda, N. 2001, in ASP Conf. Ser. 238, Astronomical Data Analysis Software and Systems X, ed. F. R. Harnden Jr., F. A. Primini, & H. E. Payne (San Francisco: ASP), 269
Lupton, R. H., Gunn, J. E., & Szalay, A. S. 1999, AJ, 118, 1406
Maness, H., et al. 2007, ApJ, 669, 1024
Maraston, C. 2005, MNRAS, 362, 799
Masjedi, M., Hogg, D. W., & Blanton, M. R. 2008, ApJ, 679, 260
Masjedi, M., et al. 2006, ApJ, 644, 54
McCarthy, P. J., et al. 2004, ApJ, 614, L9
McCrady, N., Gilbert,A. M., & Graham, J. R. 2003, ApJ, 596, 240
McIntosh, D. H., Guo, Y., Hertzberg, J., Katz, N., Mo, H. J., van den Bosch, F. C., & Yang, X. 2007, preprint (arXiv: 0710.2157)
McIntosh, D. H., Zabludoff, A. I., Rix, H.-W., & Caldwell, N. 2005, ApJ, 619, 193
Nelan, J. E., Smith, R. J., Hudson, M. J., Wegner, G. A., Lucey, J. R., Moore, S. A. W., Quinney, S. J., & Suntzeff, N. B. 2005, ApJ, 632, 137
Oke, J. B., & Gunn, J. E. 1983, ApJ, 266, 713
Papovich, C., Dickinson, M., Giavalisco, M., Conselice, C. J., & Ferguson, H. C. 2005, ApJ, 631, 101
Pier, J. R., Munn, J. A., Hindsley, R. B., Hennessy, G. S., Kent, S. M., Lupton, R. H., & Ivezić, Ž. 2003, AJ, 125, 1559
Pimbblet, K. A., Smail, I., Edge, A. C., O'Hely, E., Couch, W. J., & Zabludoff, A. I. 2006, MNRAS, 366, 645
Rieke, G. H., Loken, K.,Rieke, M. J., & Tamblyn, P. 1993, ApJ, 412, 99
Rines, K., Finn, R., & Vikhlinin, A. 2007, ApJ, 665, L9
Roll, J. B., Fabricant, D. G ., & McLeod, B. A. 1998, Proc. SPIE, 3355, 324
Salpeter, E. E. 1955, ApJ, 121, 161
Schmidt, M. 1968, ApJ, 151, 393
Schlegel, D. J., Finkbeiner, D. P., & Davis, M. 1998, ApJ, 500, 525
Seo, H.-J., Eisenstein, D. J., & Zehavi, I. 2007, preprint (arXiv: 0712.1643)
Smith, J. A., et al. 2002, AJ, 123, 2121
Spergel, D. N., et al. 2007, ApJS, 170, 377
Stolte, A., Brandner, W., Grebel, E. K., Lenzen, R., & Lagrange, A.-M. 2005, ApJ, 628, L113
Stoughton, C., et al. 2002, AJ, 123, 485
Strauss, M. A., et al. 2002, AJ, 124, 1810
Thomas, D., Maraston, C., Bender, R., & Mendes de Oliveira, C. 2005, ApJ, 621, 673
Trager, S. C., Faber, S. M., Worthey, G., & González, J. J. 2000, AJ, 120, 165
Tran, K.-V. H., van Dokkum, P., Franx, M., Illingworth, G. D., Kelson, D. D., & Schreiber, N. M. F. 2005, ApJ, 627, L25
Tucker, D. L., et al. 2006, Astron. Nachr., 327, 821
van Dokkum, P. G. 2005, AJ, 130, 2647
———. 2008, ApJ, 674, 29
van Dokkum, P. G., Franx, M., Fabricant, D., Kelson, D. D., & Illingworth, G. D. 1999, ApJ, 520, L95
Visvanathan, N., & Sandage, A. 1977, ApJ, 216, 214
Wake, D. A., Collins, C. A., Nichol, R. C., Jones, L. R., & Burke, D. J. 2005, ApJ, 627, 186
Wake, D. A., et al. 2006, MNRAS, 372, 537
———. 2008, MNRAS, 387, 1045
White, M., Zheng, Z., Brown, M. J. I., Dey, A., & Jannuzi, B. T. 2007, ApJ, 655, L69
Willmer, C. N. A., et al. 2006, ApJ, 647, 853
York, D. G., et al. 2000, AJ, 120, 1579
Zehavi, I., et al. 2005, ApJ, 621, 22